Chapter 3

Probing Barrier Distributions with Quasi-Elastic Scattering

3.1 Derivation of a Barrier Distribution Representation

The experimental distributions $D^{fus}(E)$ discussed in Section 1.5.3, which are representative of the potential barrier distribution encountered in a reaction, are direct evidence of the coupling of the fusing nuclear binary system to its internal degrees of freedom. Fusion results from transmission over the barrier and the flux which is not transmitted is reflected. At barrier energies this reflected flux is dominated by quasi-elastic scattering, such as elastic and inelastic scattering and transfer reactions. Since the sum of the transmitted and the reflected flux is conserved, one may expect that the coupling terms in the Hamiltonian affect not only fusion but also the quasi-elastic scattering. Indeed, individual quasi-elastic scattering channels have been described successfully with coupled-channels calculations for a long time. In addition, for many systems correlations have been observed between excitation functions for quasi-elastic scattering channels and for fusion, as has been pointed out in Section 1.6.2. It may therefore be hoped that the distribution of potential barriers is evident in the excitation functions measured for the quasi-elastic scattering reaction channels.

On the basis of the coupled-channels model, it has been suggested[1,2] that some information about the distribution of potential barriers of a reaction might be contained in the backward angle excitation functions for the combined quasi-elastic scattering yield of elastic and inelastic scattering and transfer reactions. Following this suggestion, this chapter describes the derivation and test of a technique which allows representations of the barrier distribution to be extracted from precise measurements of quasi-elastic scattering.

3.1.1 The Case of a Single Barrier

Classically, for a single potential barrier B_k and head-on collisions, i.e. the scattering angle $\theta = 180°$, there is a direct relationship between the differential fusion cross section $d\sigma^{fus}(E)$ and the quasi-elastic scattering differential cross section $d\sigma^{qel}(E)$. Since any loss from the elastic channel, which in this idealized case is the only quasi-elastic channel, contributes directly to fusion, this is a consequence of flux

[1] A.T. Kruppa *et al.*, Nucl. Phys. A **560** (1993) 845.

[2] M.V. Andres, N. Rowley, M.A. Nagarajan, Phys. Lett. B **202** (1988) 292.

conservation as expressed by

$$\mathcal{T}(E) + \mathcal{R}(E) \equiv 1 \tag{3.1}$$

where $\mathcal{T}(E)$ and $\mathcal{R}(E)$ are the transmission and reflection coefficients, respectively. Whilst the reflection coefficient is equal to the ratio of the differential cross sections for quasi-elastic and Rutherford scattering $d\sigma^{qel}/d\sigma^{R}(E)$, the transmission coefficient $\mathcal{T}(E)$ may be written as the first differential of the product of energy and total fusion cross section $E\sigma^{fus}$ with respect to energy, as it has been shown in Section 1.5.3. Thus

$$\mathcal{R}(E) = \frac{d\sigma^{qel}}{d\sigma^{R}}(E, \theta = 180°) \tag{3.2}$$

and

$$\mathcal{T}(E) = \frac{1}{\pi R_0^2} \frac{d}{dE} \left[E\sigma^{fus}(E) \right] \tag{3.3}$$

where R_0 is the fusion radius. According to Equation 1.56 further differentiation of Equation 3.3 with respect to energy yields

$$\frac{d\mathcal{T}}{dE} = \frac{1}{\pi R_0^2} \frac{d^2}{dE^2} \left[E\sigma^{fus}(E) \right] = \delta(E - B_k) = D(E, B_k) \tag{3.4}$$

The function $D(E, B_k)$ is the barrier distribution of the system which for a single barrier is simply a δ-function at the barrier height B_k. Combining the Equations 3.1, 3.2, 3.3 and 3.4 it follows that

$$D(E, B_k) = \frac{d\mathcal{T}}{dE} = -\frac{d\mathcal{R}}{dE} = -\frac{d}{dE} \left[\frac{d\sigma^{qel}}{d\sigma^{R}}(E, \theta = 180°) \right] \tag{3.5}$$

Thus, classically for a single barrier the barrier distribution $D(E, B_k)$ can be obtained by differentiating $d\sigma^{qel}/d\sigma^{R}(E)$ at 180° with respect to energy.

In the quantum mechanical description the effects of tunnelling prevent the barrier distribution $D(E, B_k)$ from being recovered from $E\sigma^{fus}$. However, as derived in Section 1.5.3, the second differential of $E\sigma^{fus}$ with respect to energy yields the distribution

$$D^{fus}(E) = \frac{d^2}{dE^2} \left[E\sigma^{fus}(E) \right] = \pi R_0^2 G^{fus}(E, B_k) \tag{3.6}$$

which is representative of the barrier distribution $D(E, B_k)$, because $G^{fus}(E, B_k)$ which is defined in Equation 1.57 is a narrowly peaked function. Since the function

$$D^{qel}(E) = -\frac{d}{dE} \left[\frac{d\sigma^{qel}}{d\sigma^{R}}(E, \theta = 180°) \right] = G^{qel}(E, B_k) \tag{3.7}$$

is also narrowly peaked (see Section 3.1.3), it defines an alternative representation of the barrier distribution for the trivial case of a single barrier.

3.1.2 Extension to Multiple Barriers

It is not immediately apparent that the above derivation can be extended to situations where several barriers are involved. For a distribution of several barriers the reflected flux comprises the elastic scattering channel ($j = 0$) and a series of quasi-elastic reaction channels ($j = 1, 2, .., n$), so that

$$\frac{d\sigma^{qel}}{d\sigma^R}(E,\theta) = \sum_{j=0}^{n} \frac{d\sigma_j}{d\sigma^R}(E,\theta) \tag{3.8}$$

As shown in Section 1.5.3, multi-dimensional barrier penetration may be described within the simplified coupled-channels model which considers coupling to a finite number of states but neglects their excitation energies (sudden approximation) and spins (iso-centrifugal approximation). According to Equation 1.48 the elements of the scattering matrix S_j^ℓ for the physical reaction channels are then unitary transformations of the elements of the scattering matrix $\bar{S}_k^\ell$ for the eigen-channels ($k = 0, 1, .., n$) and

$$S_j^\ell = U_{jk} U_{0k} \bar{S}_k^\ell \tag{3.9}$$

The scattering amplitudes $f_j(E,\theta)$ for the physical reaction channels as given by Equation 1.64 can then be expressed as

$$f_j(E,\theta) = \frac{\lambda}{2i} \sum_{\ell,k} (2\ell+1) P_\ell(\cos\theta) \exp[2i\sigma_k^\ell] U_{jk} U_{0k} \bar{S}_k^\ell \tag{3.10}$$

where the σ_k^ℓ are the Coulomb phases in the eigen-channels and λ is the reduced de Broglie wave length. The partial wave sum in Equation 3.10 does not converge because of the elastic channel and it is common to separate out the Coulomb amplitude as expressed in Equation 1.65. It is also possible to use suitable convergence factors[3]. In the following such factors may be considered to be implicitly included. The Equations 3.10 are only strictly valid in the case when the spins of the excited states are ignored. In reality the coupling of an entrance-channel ℓ to a final-channel ℓ' may change the phase-relations between different scattering amplitudes.

Using Equations 1.63 and 3.10, the quasi-elastic scattering cross section relative to Rutherford scattering can be expressed as

$$\frac{d\sigma^{qel}}{d\sigma^R}(E,\theta) = \frac{1}{d\sigma^R} \sum_{j,k,l=0}^{n} \left| \frac{\lambda}{2i} \sum_{\ell} (2\ell+1) P_\ell(\cos\theta) \right|^2 \exp[2i(\sigma_k^\ell + \sigma_l^\ell)] U_{jk} U_{0k} \bar{S}_k^\ell U_{jl}^* U_{0l}^* \bar{S}_l^\ell \tag{3.11}$$

[3]N. Rowley, J. Phys. A: Math. and Gen. **11** (1978) 1545.

Using the relation 1.50 this simplifies to

$$\frac{d\sigma^{qel}}{d\sigma^R}(E,\theta) = \frac{1}{d\sigma^R}\sum_{k=0}^{n} W_k \left|\frac{\lambda}{2i}\sum_{\ell}(2\ell+1)P_\ell(\cos\theta)\exp[2i\sigma_k^\ell]\bar{S}_k^\ell\right|^2 \tag{3.12}$$

where the $W_k \equiv |U_{0k}|^2$ are the weights with which the different eigen-channels k contribute to the quasi-elastic differential scattering cross section. It follows that for a particular angle θ

$$\frac{d\sigma^{qel}}{d\sigma^R}(E) = \sum_{k=0}^{n} W_k \frac{d\sigma_k}{d\sigma^R}(E) \tag{3.13}$$

where $d\sigma_k$ is the differential cross section for the eigen-channel k. Thus, in the eigen-channel model the quasi-elastic differential cross section is a weighted sum of the eigen-channel differential cross sections. It should be noted that this equation is equivalent to Equation 1.51 for the fusion cross section. One important difference is indicated by the phase terms $\exp[2i\sigma_k^\ell]$ which do not occur in Equation 1.51. As a consequence of the iso-centrifugal and sudden approximations the scattering from each eigen-barrier k proceeds with a well defined phase, although it contains contributions from all physical scattering channels. In reality, the different angular momenta and energies of these physical channels may lead to some *de-phasing*, which could distort the cross sections $d\sigma_k/d\sigma^R(E)$ associated with the eigen-channels.

The differentiation of Equation 3.13 with respect to energy yields the distribution

$$D^{qel}(E) \equiv -\frac{d}{dE}\left[\frac{d\sigma^{qel}}{d\sigma^R}(E)\right] = -\sum_{k=0}^{n} W_k \frac{d}{dE}\left[\frac{d\sigma_k}{d\sigma^R}\right] = \sum_{k=0}^{n} W_k G^{qel}(E,B_k) \tag{3.14}$$

where for θ close to 180° the $G^{qel}(E,B_k)$ are narrowly peaked functions (see Section 3.1.3). Consequently, similar to $D^{fus}(E)$, the distribution $D^{qel}(E)$ is a representation of the barrier distribution $D(E,B_k)$. The question arises if, as for $D^{fus}(E)$, the barrier structure is retained in the representation $D^{qel}(E)$, when the approximations implicit in its derivation are relaxed.

3.1.3 Application to Calculated Excitation Functions

The validity of the approximations in Sections 3.1.1 and 3.1.2 has been tested by performing exact coupled-channels calculations with the code ECIS[4] for an arbitrary

[4] J. Raynal, *Computing as a Language of Physics*, I.A.E.A Vienna (1972) 281.

binary system. From the theoretical excitation functions for fusion and quasi-elastic scattering at $\theta = 180°$ the distributions $D^{fus,qel}(E)$ were extracted by differentiation. The differentiation was approximated for fusion with the point-difference formula given in Equation 1.60 and for quasi-elastic scattering with the point-difference formula

$$D^{qel}(E) \simeq -\frac{d\sigma^{qel}/d\sigma^{R}(E + 0.5\Delta E) - d\sigma^{qel}/d\sigma^{R}(E - 0.5\Delta E)}{\Delta E} \tag{3.15}$$

In both cases an energy step length of $\Delta E = 2$ MeV was used. The distributions $D^{fus}(E)$ were divided by the asymptotic classical fusion cross section πR_0^2 to facilitate the comparison with $D^{qel}(E)$. The values of πR_0^2 were determined by applying Equation 3.3 at high energies where $T(E) \rightarrow 1$.

Initially a reaction featuring a single barrier was considered, which was simulated by including in the calculations only the elastic channel and an absorptive potential. The total reaction cross section was taken to be equal to $\sigma^{fus}(E)$. The resulting distributions $D^{fus}(E)$ and $D^{qel}(E)$ are compared in Figure 3.1(a). They have very similar widths and shapes.

A case with two well separated barriers was simulated by coupling the elastic channel to a quadrupole vibrational state at high excitation energy. The fusion cross section was taken as the difference between the total reaction and the total inelastic cross section, while the quasi-elastic differential cross section was taken as the sum of those for elastic and inelastic scattering. The distributions $D^{fus}(E)$ and $D^{qel}(E)$ extracted from this calculation are shown in Figure 3.1(b). Again they are in good agreement.

Calculations were also performed for a system where one of the nuclei is deformed. They incorporated the first five rotational states of the deformed nucleus and assumed a positive quadrupole and a negative hexadecapole deformation. The overall shapes of $D^{fus}(E)$ and $D^{qel}(E)$ are again similar, as it is shown in Figure 3.1(c). However, the interference of different scattering amplitudes now appears to distort $D^{qel}(E)$ in an oscillatory manner, which is indicative of Fresnel diffraction. Nonetheless, the structure of the barrier distribution is still apparent.

Experimentally it is difficult to measure scattering excitation functions at a laboratory angle $\theta_{lab} = 180°$. Therefore, the calculations of $D^{qel}(E)$ for the deformed nucleus were also performed at $\theta_{lab} = 150°$. In order to compare the shape of $D^{qel}(E, 150°)$ with that of $D^{qel}(E, 180°)$, the energy scale of the former was reduced by the centrifugal energy E_{cent}. Assuming Rutherford orbits, the centrifugal energy

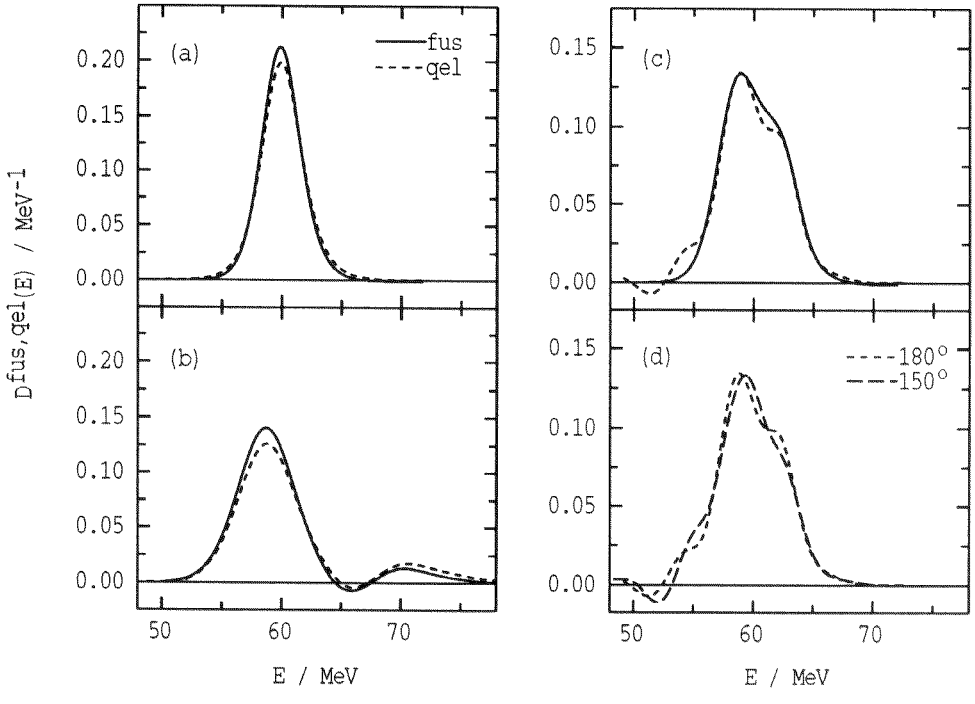

Figure 3.1: *Representations $D^{fus,qel}(E)$ of the potential barrier distribution from fusion (solid) and quasi-elastic scattering at 180° (dashed) as calculated with* ECIS *for (a) a single barrier, (b) two well separated barriers and (c) for a rotational nucleus with deformation parameters $\beta_2 = 0.3$ and $\beta_4 = -0.05$. The two representations are very similar for all three cases. Panel (d) shows $D^{qel}(E,\theta)$ at $\theta_{lab} = 180°$ and 150°. The energy scale of the 150° distribution was shifted by E_{cent}. The distributions $D^{fus}(E)$ have been divided by πR_0^2 to facilitate the comparison.*

is given by

$$E_{cent} = E_{cm}\frac{\mathrm{cosec}(\theta_{cm}/2) - 1}{\mathrm{cosec}(\theta_{cm}/2) + 1} \tag{3.16}$$

where θ_{cm} is the detection angle in the centre-of-mass system. As shown in Figure 3.1(d), the shape of $D^{qel}(E)$ changes only slightly with angle over this range. An obvious feature is that the phases of the oscillations change with detection angle, supporting the conclusion that they are associated with diffractive effects in scattering. Calculated distributions at intermediate angles lie within the limits of these two curves. The oscillations have only small amplitudes and do not destroy the barrier structure in $D^{qel}(E)$. However, for detection angles $\theta_{lab} \lesssim 140°$ the amplitude of the oscillations is found to increase rapidly. This suggests that measurements of the quasi-elastic scattering excitation functions at the most backward angles are

best suited to extract the distributions $D^{qel}(E)$ with a minimum of distortion due to diffraction.

In summary, the exact coupled-channels calculations presented in this section support the idea that a representation of the barrier distribution may be extracted from quasi-elastic scattering data. The calculated representations $D^{fus}(E)$ and $D^{qel}(E)$ of the barrier distribution appear to be very similar. There is, however, an important difference between them. They propagate experimental uncertainties differently. For a fixed relative experimental uncertainty δ of the cross sections, the uncertainty of $D^{fus}(E)$ increases with energy and cross section, as given by Equation 1.61. This leads to large uncertainties for $D^{fus}(E)$ at higher energies. In contrast, from Equation 3.15 it follows that for $D^{qel}(E)$ the uncertainty is approximately given by

$$\Delta D^{qel} \simeq \frac{\delta\sqrt{2}}{\Delta E}\left[\frac{d\sigma^{qel}}{d\sigma^{R}}(E)\right] \tag{3.17}$$

Consequently, for this representation the uncertainty decreases with energy in the barrier region, where the quasi-elastic cross section falls rapidly.

The large experimental uncertainties at higher energies are a major problem in the extraction of the barrier structure from $D^{fus}(E)$. This is demonstrated in Figure 3.2 for two experimental distributions $D^{fus}(E)$. Even with a precision of the fusion cross sections corresponding to $\delta = 0.01$, the distributions $D^{fus}(E)$ are not well defined at higher energies. At energies above the average barrier height B_0 the fusion data cannot be used to distinguish between the two calculations which are also shown in the figure[5]. An alternative representation of the barrier distribution as given by $D^{qel}(E)$ which is better defined at high energies would therefore be extremely useful to extract the barrier structure in this energy range.

3.2 The Systems $^{16}O + ^{96}Zr$, $^{144,154}Sm$ and ^{186}W

Although for many systems quasi-elastic angular distributions are well documented in the literature, excitation functions have only rarely been measured and the existing data are not precise enough to extract meaningful distributions $D^{qel}(E)$. In order to investigate the technique which has been derived in the previous sections, precise quasi-elastic scattering excitation functions have therefore been measured in this work for the systems $^{16}O + ^{92}Zr$, ^{144}Sm, ^{154}Sm and ^{186}W. These reactions were

[5] J.R. Leigh *et al.*, Phys. Rev. C 47 (1993) R437.

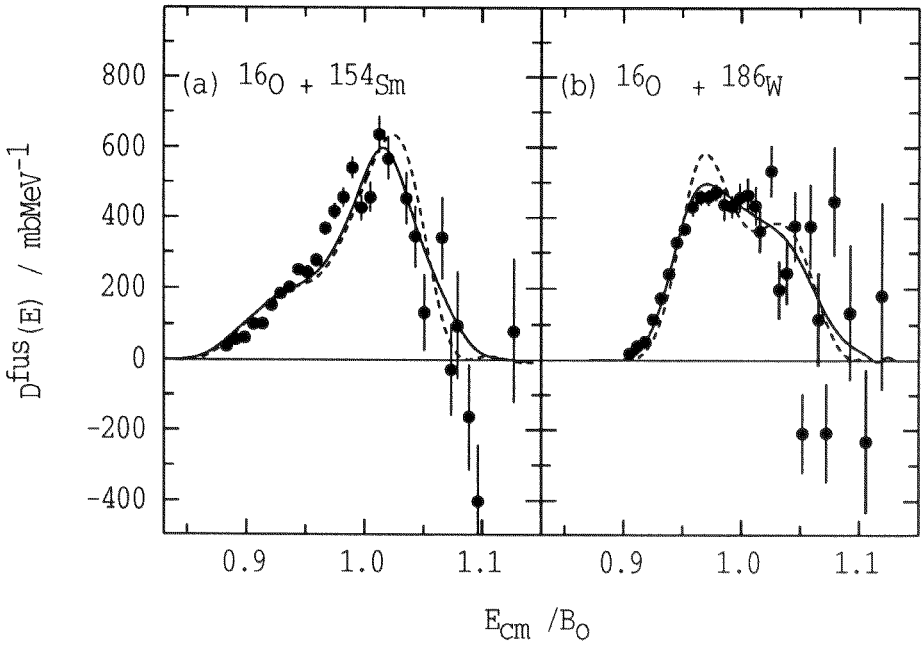

Figure 3.2: *Experimental representations $D^{fus}(E)$ of the distribution of potential barriers are compared with model calculations for (a) ^{16}O + ^{154}Sm and (b) ^{16}O + ^{186}W. The dashed curves result from calculations which include only the effects of deformation. The solid curves represent calculations which in addition include weak couplings to vibrational 2^+ and 3^- states of the target nuclei. The energies are in units of the average barrier height B_0.*

selected because the experimental distributions $D^{fus}(E)$ are known[6–10], so that a comparison of $D^{fus}(E)$ and $D^{qel}(E)$ is possible.

3.2.1 Excitation Functions

The measurements were carried out with ^{16}O beams from the electrostatic tandem accelerator at the Australian National University, in the energy range E_{lab} = 35 – 85 MeV. The quasi-elastic scattering excitation functions were measured at backward angles relative to Rutherford scattering as has been described in Section 2.4. The detection angles for ^{16}O + ^{92}Zr were $\theta_{lab} = 143°$ and 155°, while for

[6]J.X. Wei *et al.*, Phys. Rev. Lett. **67** (1991) 3368.

[7]R.C. Lemmon *et al.*, Phys. Lett. B **316** (1993) 32.

[8]C.R. Morton *et al.*, Phys. Rev. Lett. **72** (1994) 4074.

[9]J.C. Mein *et al.*, *to be published.*

[10]J.R. Leigh *et al.*, Phys. Rev. C **52** (1995) 3151.

$^{16}O + ^{144}Sm$ they were $\theta_{lab} = 143°, 155°$ and 170°. For the systems $^{16}O + ^{154}Sm$ and $^{16}O + ^{186}W$, the detection angle was $\theta_{lab} = 170°$.

The experimental set-up allowed separation of the atomic numbers of the scattered projectile-like nuclei. In addition, for the ^{92}Zr and ^{144}Sm targets, the pure elastic scattering was clearly resolved from inelastic and transfer scattering in the spectra. This allowed the elastic scattering differential cross sections to be extracted for these systems. For the other two reactions the elastic peak was contaminated by inelastic scattering from low-lying rotational target states. The analysis of the experimental data yielded excitation functions for inelastic and transfer channels with $Z = 6, 7, 8$ as well as elastic scattering. The quasi-elastic yield was taken as the sum of all those channels. The measured excitation functions are documented in the Appendix in Tables A.1–A.7 and they are shown in Figures 3.3 and 3.4.

For all four systems the quasi-elastic excitation functions $d\sigma^{qel}/d\sigma^{R}(E)$ show a smooth, monotonic decrease with energy. However, the rate of decrease for the reactions involving the deformed target nuclei ^{154}Sm and ^{186}W (Figure 3.3) is different compared to the reactions with the two lighter, non-deformed target nuclei ^{92}Zr and ^{144}Sm (Figure 3.4). While the latter fall from $d\sigma^{qel}/d\sigma^{R} = 0.9$ to 0.1 within $\sim$ 6 MeV, the excitation functions for the deformed target nuclei fall more slowly within $\sim$ 10 MeV, as might be expected when a wide range of potential barriers is present in a reaction. Hence, from this qualitative comparison, the quasi-elastic excitation functions at backward angles appear to have some sensitivity to the fusion barrier distribution. A similar, but less pronounced dependency of the elastic scattering excitation function on the shape of the reactants has previously been observed[11] for the reactions of the spherical ^{6}Li and the deformed ^{7}Li with ^{58}Ni and other target nuclei.

3.2.2 Comparison of Quasi-Elastic and Fusion Data

The quasi-elastic scattering excitation functions have been transformed into the distributions $D^{qel}(E)$ using an energy step length $\Delta E_{lab} = 2$ MeV in the point-difference formula (3.15). For $^{16}O + ^{92}Zr$ some data points have been derived with $\Delta E_{lab} = 1$ MeV and 3 MeV. The resulting distributions $D^{qel}(E)$ are shown in Figure 3.5. The energy scales for each angle have been reduced by the centrifugal energy, as given by Equation 3.16.

The experimental distributions $D^{qel}(E)$ show significant differences for the four

[11] W. Dreves *et al.*, Phys. Lett. B 78 (1978) 36.

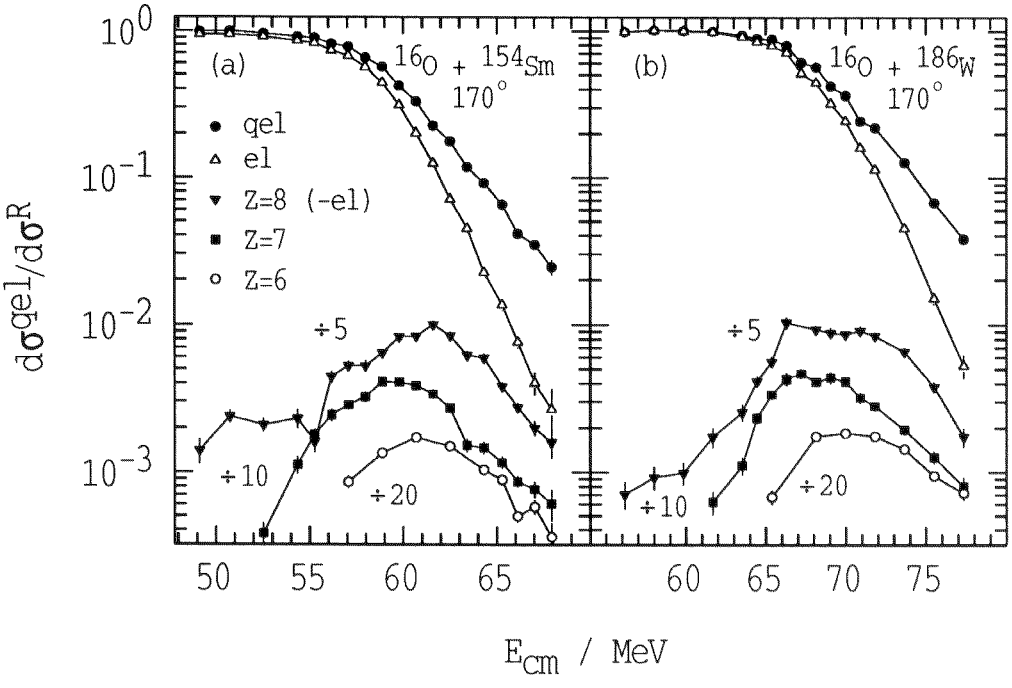

Figure 3.3: *The ratio of the measured differential quasi-elastic (qel), elastic (el) and the Z=8, Z=7, Z=6 scattering and transfer cross sections relative to Rutherford scattering for (a) ^{16}O + ^{154}Sm and (b) ^{16}O + ^{186}W at θ_{lab} = 170°. The excitation function for Z=8 does not include the elastic scattering. It should be noted that for both systems the excitation function labelled 'el' also contains some inelastic scattering from low-lying rotational target states which could not be resolved. Some of the excitation functions have been divided by 5, 10 or 20, as indicated. The yield of nuclei with Z = 8 was subtracted by the yield for elastic scattering, as indicated by (−el).*

reactions studied, suggesting that they indeed reflect the barrier distribution of the reaction. The differences for the reactions with the two samarium isotopes are particularly striking. There is already significant barrier strength at $E_{cm} \sim 50$ MeV for the deformed ^{154}Sm case and this distribution rises slowly with increasing energy in contrast to the ^{144}Sm distribution which rises steeply starting at a higher energy.

The distributions $D^{qel}(E)$ of all four reactions are compared with the corresponding distributions $D^{fus}(E)$ in Figure 3.6 for the same energy step length ΔE_{lab} = 2 MeV. The experimental values for $D^{fus}(E)$ have been divided by the classical fusion cross section πR_0^2 as determined with Equation 3.3 by fitting the experimental high energy cross sections where the transmission approaches unity. The values of πR_0^2 determined for ^{16}O+ ^{92}Zr, ^{144}Sm, ^{154}Sm and ^{186}W are 2940 mb,

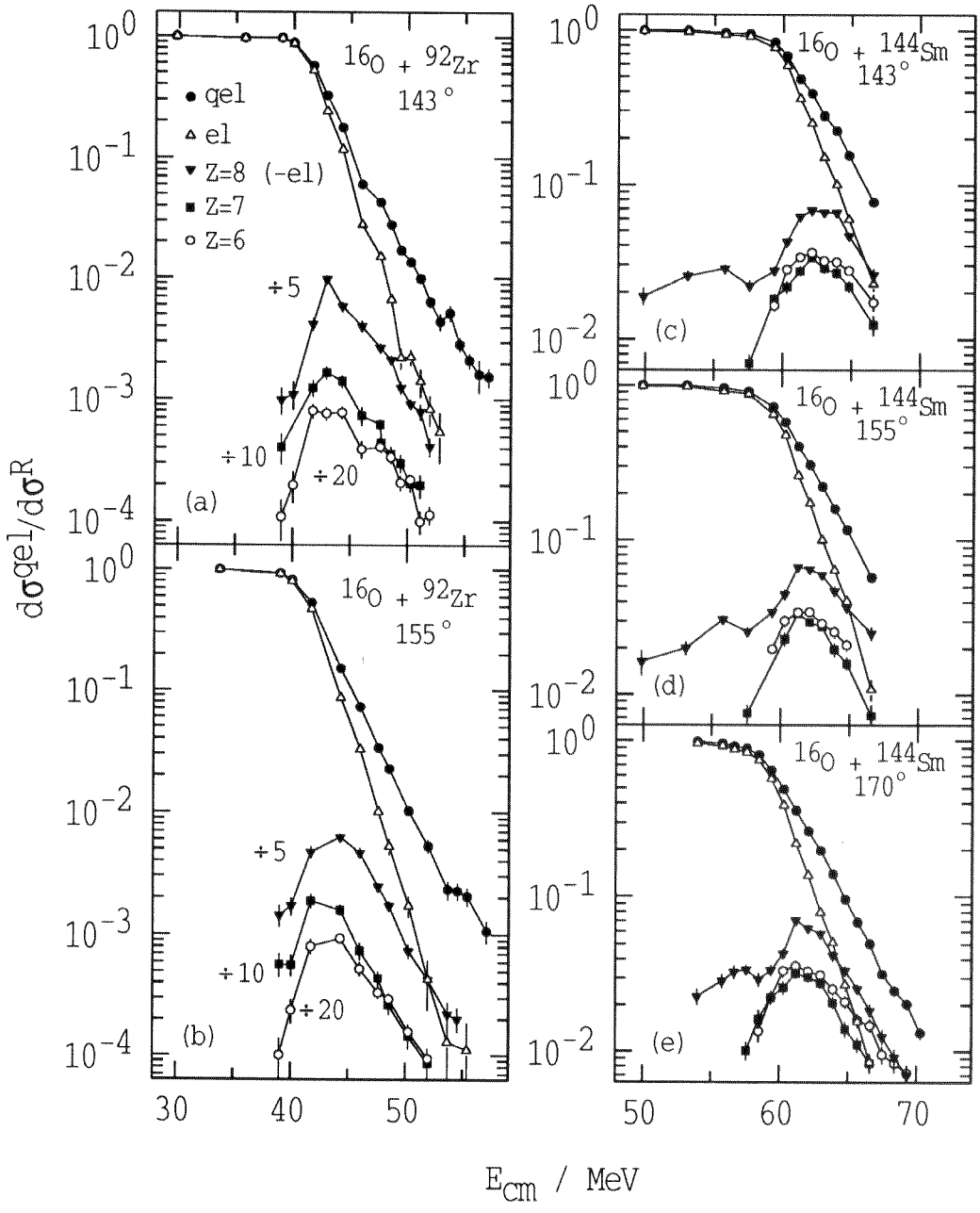

Figure 3.4: *The ratio of the differential quasi-elastic (qel), elastic (el) and the Z=8, Z=7, Z=6 scattering and transfer cross sections relative to Rutherford scattering for* $^{16}O + ^{92}Zr$ *and* ^{144}Sm. *The detection angles* θ_{lab} *are indicated. The yield of nuclei with* $Z = 8$ *was subtracted by the yield for elastic scattering, as indicated by (−el).*

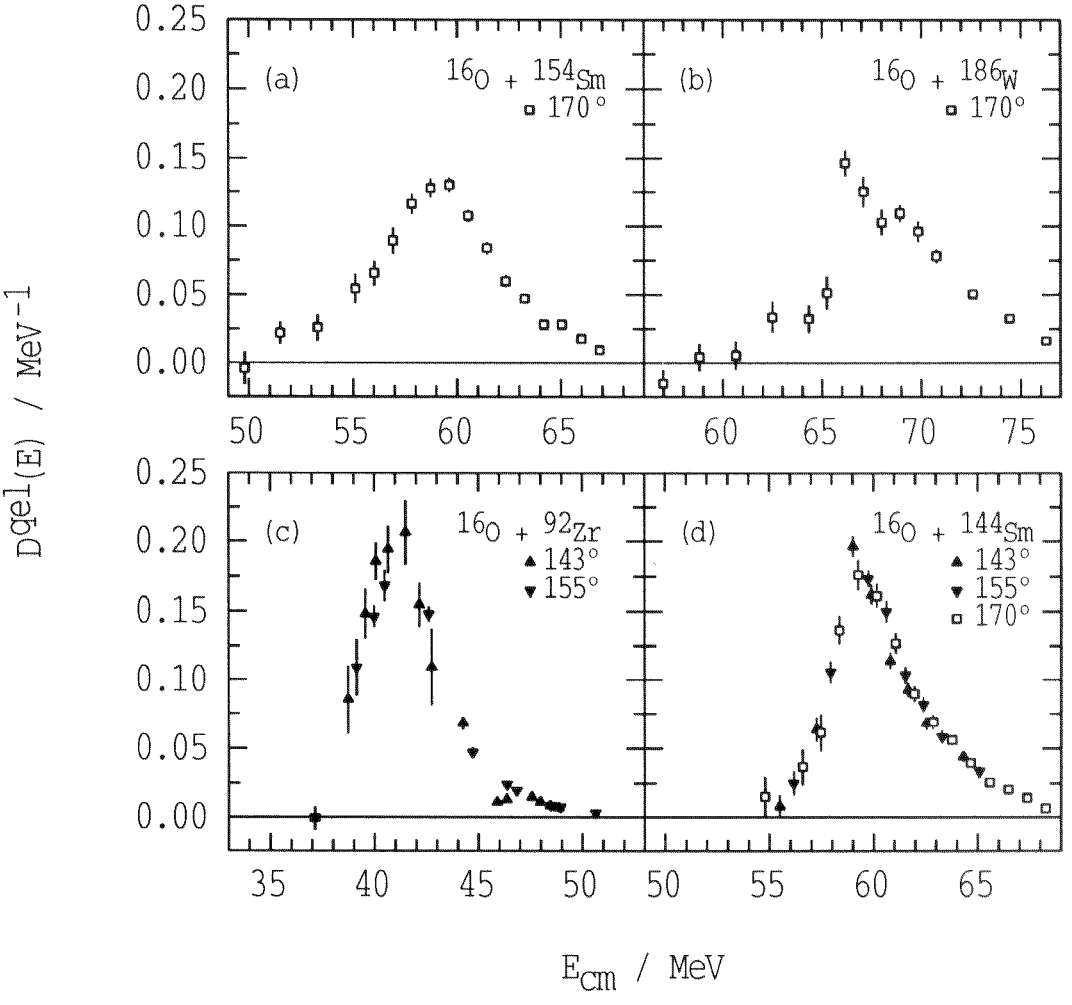

Figure 3.5: *The representations $D^{qel}(E)$ of the barrier distribution as determined for the systems indicated. As in the following figures, the centre-of-mass energies E_{cm} have been reduced by E_{cent}. The distributions $D^{qel}(E)$ reflect the contrast between the wide range of fusion barriers expected for deformed target nuclei (a,b) and the narrow barrier distributions expected for the non-deformed target nuclei (c,d).*

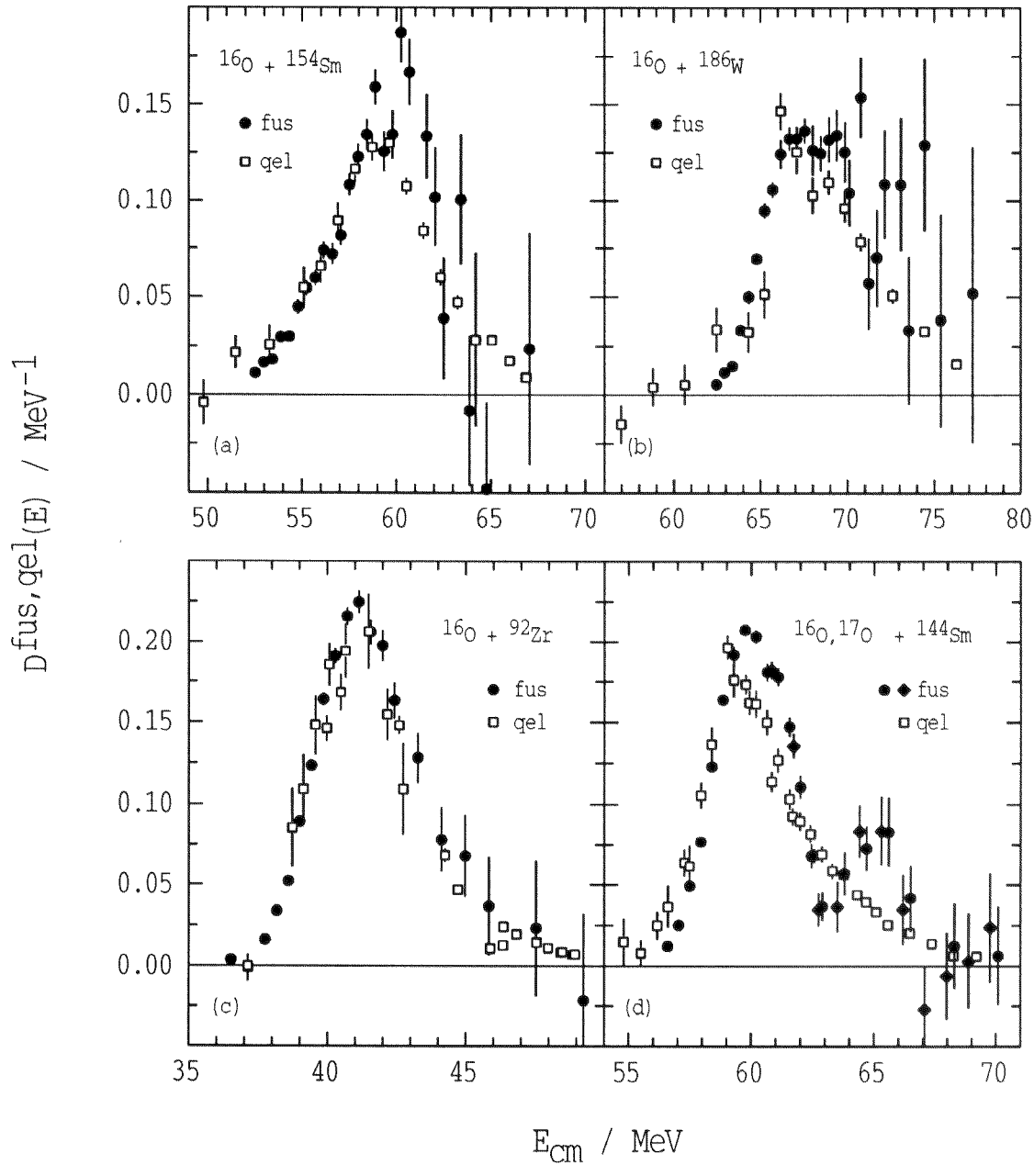

Figure 3.6: *The distributions $D^{qel}(E)$ and $D^{fus}(E)$ as extracted from experimental data for the systems indicated in the figure. In (d) $D^{fus}(E)$ is also shown at high energies for an ^{17}O projectile (diamonds). In (a–c) the distributions are consistent with each other. In (d) established structure at high energy in $D^{fus}(E)$ for the ^{144}Sm target is not seen in $D^{qel}(E)$. The distributions $D^{fus}(E)$ have been divided by πR_0^2 to facilitate the comparison.*

3480 mb, 3400 mb and 3470 mb, respectively.

For the target nuclei ^{154}Sm, ^{186}W and ^{92}Zr the distributions $D^{fus}(E)$ and D^{qel}, shown in Figure 3.6(a–c), are consistent with each other. For the deformed target nuclei ^{154}Sm and ^{186}W there is an indication at lower energies in $D^{qel}(E)$ of the oscillatory behaviour predicted by the calculations shown in Figure 3.1(c,d).

However, $D^{qel}(E)$ is different from $D^{fus}(E)$ for the ^{144}Sm target, as shown in Figure 3.6(d). For ^{16}O + ^{144}Sm the distribution $D^{fus}(E)$ shows a distinct peak about 5 MeV above the main barrier whilst this is absent from $D^{qel}(E)$. This second, high energy barrier in $D^{fus}(E)$ has also been observed for the system ^{17}O + ^{144}Sm. For both reactions it has been explained[12] as arising from couplings to the inelastic channels associated with the excitations of the lowest energy 2^+ and 3^- states in the ^{144}Sm target nucleus.

The failure of $D^{qel}(E)$ to reproduce this established and distinct high energy barrier in $D^{fus}(E)$ and the similar slow fall of $D^{qel}(E)$ at higher energies in the other reactions gives reason to question how well $D^{qel}(E)$ represents the distribution of potential barriers. In an attempt to clarify this uncertainty the data for ^{16}O + ^{144}Sm have been studied in more detail.

3.2.3 Detailed Analysis of ^{16}O + ^{144}Sm

The experimental results for ^{16}O + ^{144}Sm have been analysed more quantitatively by fitting the distributions $D^{fus}(E)$ and $D^{qel}(E)$. A functional form for $D^{fus}(E)$ can be obtained within the eigen-channel model as discussed in Section 1.5.3. It may be assumed that the fusion radius R_0 is constant and that the barrier shape is parabolic with a curvature $\hbar\omega_0$, so that with Equations 1.57 and 1.58 $D^{fus}(E)$ can be expressed as

$$D^{fus}(E) = \pi R_0^2 \sum_{k=0}^{n} W_k G(E, B_k) = \pi R_0^2 \sum_{k=0}^{n} W_k \left[\left(\frac{2\pi}{\hbar\omega_0} \right) \frac{e^x}{(1+e^x)^2} \right] \qquad (3.18)$$

where $x \equiv (2\pi/\hbar\omega_0)(E - B_k)$

As in the qualitative comparison in the last section, in order to achieve a good compromise between sensitivity and accuracy, those experimental distributions $D^{fus,qel}(E)$ for ^{16}O + ^{144}Sm have been fitted, which are obtained with an energy step ΔE_{cm} = 1.8 MeV in the point-difference formulae. The reason for

[12] C.R. Morton *et al.*, Phys. Rev. Lett. **72** (1994) 4074.

	$^{16}O + {}^{144}Sm$			
	fusion		quasi-elastic	
k	B_k / MeV	W_k	B_k / MeV	W_k
0	60.0 ± 0.2	0.80 ± 0.03	59.7 ± 0.2	0.72 ± 0.06
1	65.3 ± 0.3	0.26 ± 0.09	63.7 ± 0.5	0.20 ± 0.04
ΔB / MeV	3.2 ± 0.2		3.8 ± 0.3	

Table 3.1: *The heights B_k and weights W_k of the potential barriers present in the reaction $^{16}O + {}^{144}Sm$ as extracted from two-barrier fits to the experimental distributions $D^{fus,qel}(E)$. The last line gives the width ΔB of a single peak in the distribution.*

this particular selection of data is that this energy step is comparable to the full-width-at-half-maximum of the function $G^{fus}(E, B_k)$ for $^{16}O + {}^{144}Sm$ which with[12] $\hbar\omega_0 = 4.3$ MeV and using Equation 1.59 can be calculated to be approximately 2.4 MeV for this system. The width ΔB of a single peak in the experimental distribution $D^{fus}(E)$ may then be estimated as

$$\Delta B \simeq \sqrt{(2.4 \text{ MeV})^2 + (1.8 \text{ MeV})^2} = 3 \text{ MeV} \tag{3.19}$$

This is only slightly larger than the width of $G^{fus}(E, B_k)$, so that the information loss due to the approximate nature of the differentiation is small. The ECIS calculations in Figure 3.1(a) show that the width of $G^{qel}(E, B_k)$ which represents a single peak in $D^{qel}(E)$ can be expected to be practically identical to the width of $G^{fus}(E, B_k)$. Thus, the choice of $\Delta E_{cm} = 1.8$ MeV is also sensible for the quasi-elastic data.

The free parameters of the fits to $D^{fus,qel}(E)$ were the number of barriers present ($k = 0, 1, .., n$), the barrier heights B_k and the barrier weights W_k. The barrier curvature $\hbar\omega_0$ which was assumed to be the same for all barriers, was an additional free parameter. Whereas Equation 3.18 is a valid analytical expression for $D^{fus}(E)$ within the limitations of the eigen-channel model, it is not clear to what degree this functional form reproduces $D^{qel}(E)$. In connection with $D^{qel}(E)$ the fits should therefore only be seen as approximations.

The best fits are compared with the data in Figure 3.7 and the corresponding parameters are listed in Table 3.1. The experimental distribution $D^{fus}(E)$ in Figure 3.7(a) is best reproduced with two barriers. This corresponds to $\Delta B =$

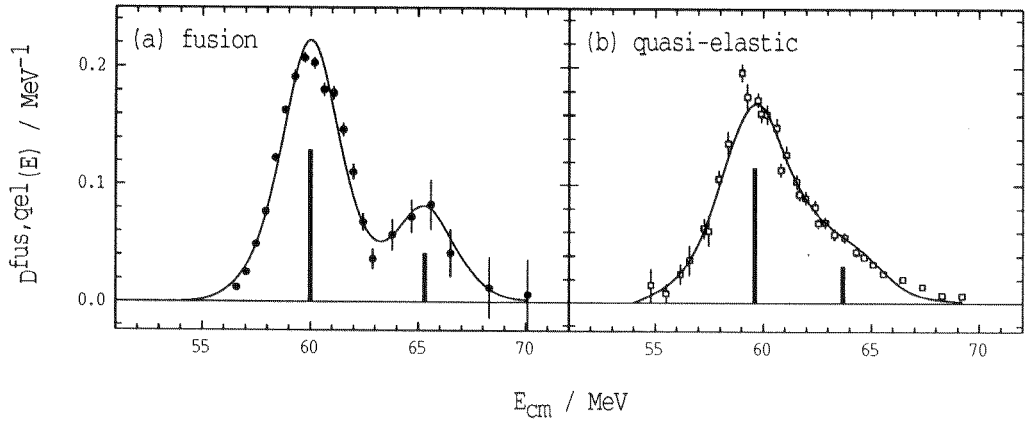

Figure 3.7: *Two-barrier fits to (a) $D^{fus}(E)$ and (b) $D^{qel}(E)$ for ^{16}O + ^{144}Sm. The barrier heights B_k and weights W_k are indicated by the vertical bars. $D^{fus}(E)$ has been divided by πR_0^2.*

3.2 ± 0.2 MeV which is in agreement with expectation. When comparing this result with the equivalent two-barrier fit to $D^{qel}(E)$ in Figure 3.7(b) the following points may be noted which confirm and detail the conclusions drawn from the qualitative comparison in Figure 3.6(d):

(i) In contrast to expectation the width ΔB is considerably larger for $D^{qel}(E)$ than for $D^{fus}(E)$.

(ii) The barrier structure extracted from $D^{qel}(E)$ is similar to the 'correct' structure represented by $D^{fus}(E)$.

(iii) The two representations of the barrier distribution agree in their prediction for the height and weight of the lower barrier.

(iv) The two representations disagree in their prediction for the height of the higher barrier.

The points (ii,iii) suggest that below the average fusion barrier height $B_0 \simeq 61$ MeV, the distribution $D^{qel}(E)$ is a correct representation of the barrier distribution. However, at higher energies the barrier structure in $D^{qel}(E)$ is distorted (iv). This is presumably due to effects which have not been taken into account in the derivation of $D^{qel}(E)$ and in the model calculations in Section 3.1.3. In addition, point (i) indicates that for experimental data the width of the function $G^{qel}(E, B_k)$ is larger

than that for $G^{fus}(E, B_k)$, thus reducing the sensitivity of $D^{qel}(E)$ in general, when compared to $D^{fus}(E)$.

The results of this comparison have been investigated further with the help of exact coupled-channels calculations using the code ECIS. These calculations were not intended to fit the data but to explain the disagreement between $D^{fus}(E)$ and $D^{qel}(E)$. A fusion excitation function was calculated which gives a good representation of the measured cross sections. This was done by using a real nuclear potential which fits the high energy fusion data in the one-dimensional model. An absorptive potential was included to ensure that passage over the barrier resulted in fusion. The potential parameters $V_0, r_0, a_0, W_0, r_w, a_w$ which were used in the calculations are 162 MeV, 1 fm, 0.9 fm, 30 MeV, 1 fm, 0.4 fm, respectively.

The calculations included vibrational coupling to the lowest 2^+ and 3^- states of ^{144}Sm at the excitation energies 1.66 MeV and 1.81 MeV. The coupling strengths were derived from the average deformation parameters $\beta_2 = 0.113$ and $\beta_3 = 0.205$ which were obtained from established B(Eλ)-values[13,14] using

$$\beta_\lambda = \frac{4\pi}{3ZR_a^\lambda}\sqrt{B(E\lambda)/e^2} \tag{3.20}$$

with the nuclear radius $R_a = 1.06A^{1/3}$ fm. Excitation of the projectile was neglected.

The results of the calculations are presented in Figure 3.8. The agreement of the theoretical and experimental fusion excitation functions and the corresponding distributions $D^{fus}(E)$ in Figure 3.8(a,b) confirm the previous result[15] that the main features of the data can be reproduced by including only coupling to the lowest 2^+ and 3^- states of ^{144}Sm in the calculations. In Figure 3.8(c) the prediction of the calculations for quasi-elastic scattering at 170° is compared with the data. The calculation follows the measured quasi-elastic scattering excitation function below $E_{cm} \simeq 64$ MeV but decreases more rapidly at higher energies. The calculated distribution $D^{qel}(E)$, in Figure 3.8(d), shows a second peak similar to $D^{fus}(E)$. The similarity between the calculated distributions $D^{fus}(E)$ and $D^{qel}(E)$, as found previously for the hypothetical coupling schemes discussed in Section 3.1.3, thus persists for this specific case. However, it is in disagreement with the experimental data.

[13]J.K. Tuli, Nucl. Data Sheets **56** (1989) 683.

[14]R. Spear, At. Data Nucl. Data Tables **42** (1989) 55.

[15]C.R. Morton *et al.*, Phys. Rev. Lett. **72** (1994) 4074.

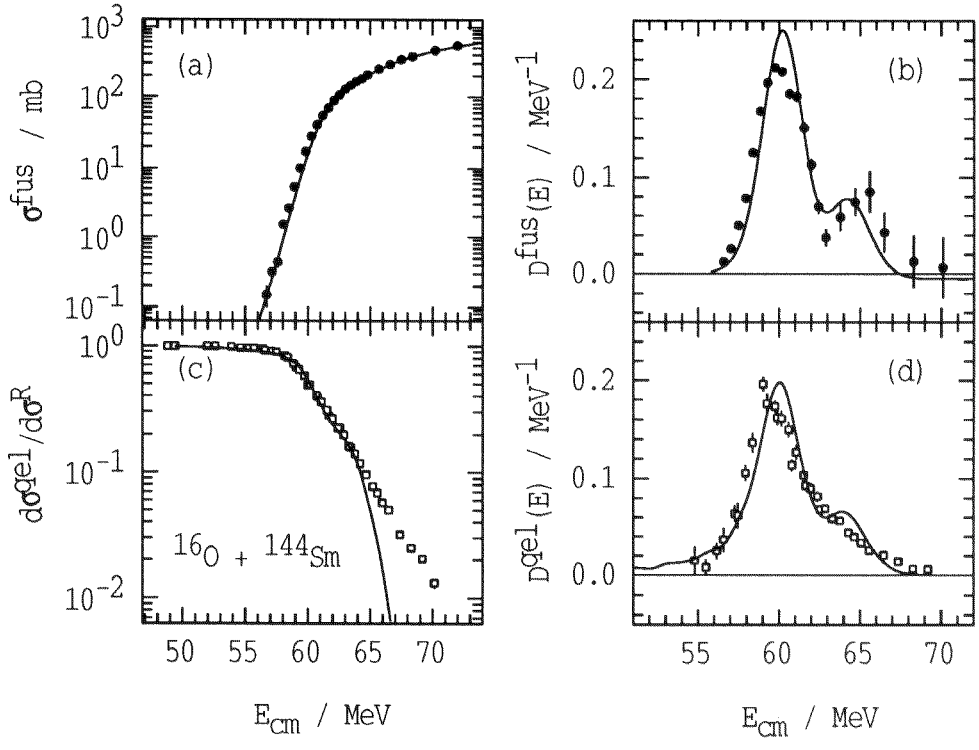

Figure 3.8: *Measured fusion (a) and 170° quasi-elastic scattering excitation functions for ^{16}O + ^{144}Sm compared with* ECIS *calculations. The corresponding distributions $D^{fus,qel}(E)$ are shown in (b) and (d). The experimental fusion excitation function and $D^{fus}(E)$ are reproduced by the calculation. For the quasi-elastic scattering excitation function the calculation drops much faster than the data at high energies. Whilst the theoretical $D^{qel}(E)$ shows the high energy barrier at 65 MeV, which is present in the experimental $D^{fus}(E)$, the experimental distribution $D^{qel}(E)$ decreases smoothly.*

A possible reason for the failure of ECIS to reproduce the measured $D^{qel}(E)$ is highlighted in Figure 3.9. In reality, the quasi-elastic yield at high energies is dominated by channels other than the two included explicitly in the ECIS calculations. This residual fraction of the observed quasi-elastic cross section increases with energy from 0 to 0.8 and proceeds mainly through transfer.

The effect of the transfer channels is demonstrated in Figure 3.10. The ECIS calculation reproduces the elastic differential cross section and predicts a sharp rise and subsequent sharp fall of the combined $(2^+,3^-)$ inelastic cross section as the energy increases. This is in qualitative agreement with the experimental data. However, between $E_{cm} = 60-65$ MeV the calculated $(2^+,3^-)$ inelastic cross section is signifi-

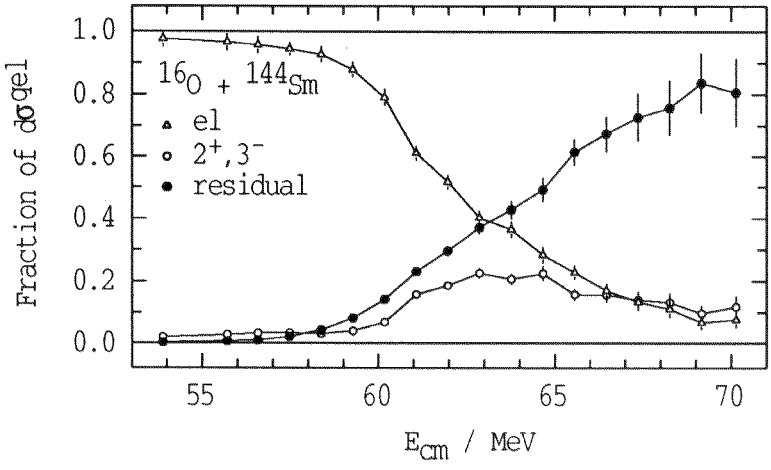

Figure 3.9: *The contributions to the experimental quasi-elastic differential cross section at 170° by the elastic, the combined (2^+,3^-) and the residual reaction channels as a function of energy.*

cantly higher than the data. This presumably occurs because in the calculation all the reflected flux has to be included in the elastic and inelastic channels whilst experimentally much of it proceeds via transfer channels. The experimental residual excitation function, which contains mainly the transfer channels, has a shape which is much wider than that of the inelastic channels and this is not accounted for by ECIS coupled-channels calculations.

The individual effects of the three specified contributions to the quasi-elastic scattering cross section on the distribution $D^{qel}(E)$ are shown in Figure 3.10(b). The ECIS calculation reproduces the elastic contribution to $D^{qel}(E)$ which does not show the high energy peak. The high energy peak in the calculation arises dominantly from the relatively strong 2^+ and 3^- channels. However, in the measured data the contribution from the residual component of the quasi-elastic cross section is relatively flat at high energies and produces a smooth decrease in $D^{qel}(E)$. Thus experimentally the high energy peak is not seen. Consequently, the disagreement between the calculated and measured distribution $D^{qel}(E)$ is largely due to the multitude of residual channels not included in the ECIS calculations, which are dominantly transfer reactions. These channels should therefore also be responsible for the distortion of the barrier distribution representation $D^{qel}(E)$. This can be understood, since transfer reactions can involve large changes in energy and angular momentum during the interaction. The assumption of quasi-elastic scat-

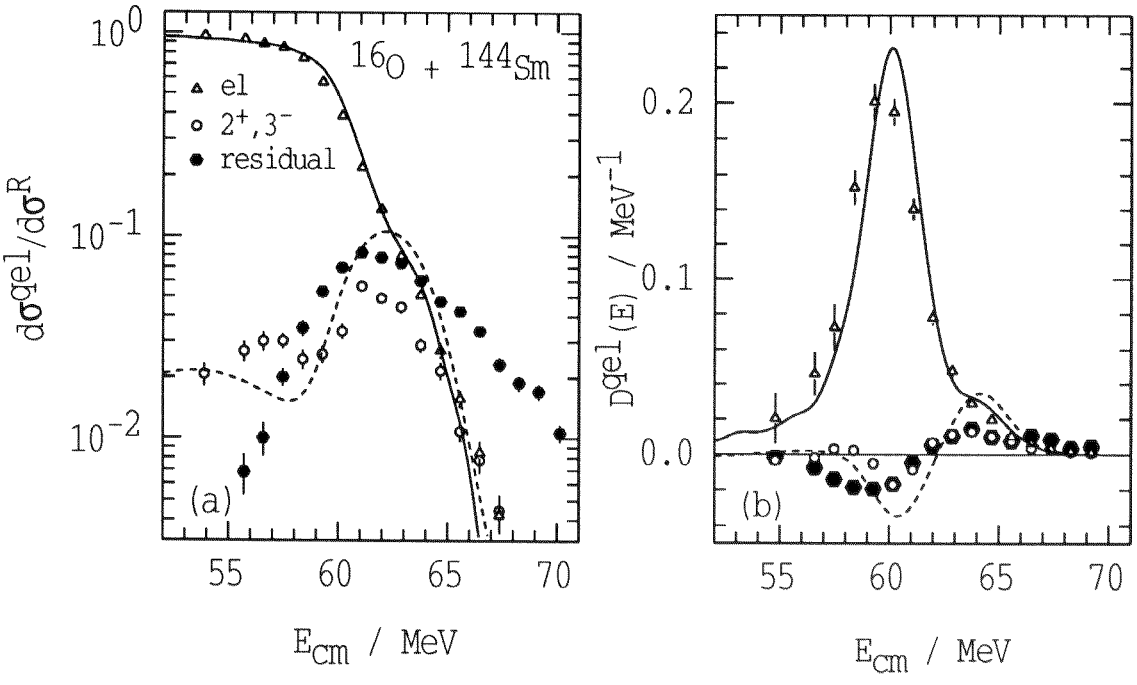

Figure 3.10: *Part (a) shows the pure elastic, the combined $(2^+,3^-)$ inelastic and the residual component of $d\sigma^{qel}/d\sigma^R(E)$. They are compared with ECIS calculations which included the elastic (solid) and the 2^+ and 3^- channels (dashed). The calculations reproduce the elastic differential cross section and predict a sharp rise and fall of the $(2^+,3^-)$ excitation function. Part (b) shows the corresponding components of $D^{qel}(E)$ and indicates that the over-prediction of the $(2^+,3^-)$ component gives rise to the second peak at 64 MeV in the* ECIS *calculation of $D^{qel}(E)$. However, in the experimental data the broad shape of the strong residual contribution to the quasi-elastic cross section causes a smooth decrease of $D^{qel}(E)$.*

tering, which is essential in the derivation of $D^{qel}(E)$, is therefore not good at the higher energies, where the reflected flux is dominated by the residual channels. In fact, instead of having a constant phase, the various physical scattering amplitudes contributing to the eigen-channels have to be expected to experience considerable de-phasing at the higher bombarding energies. The information about the barrier structure may then be lost.

3.2.4 Evidence for Coupling Effects in Transfer Channels

The observed distortion of the barrier distribution representation $D^{qel}(E)$ due to the effects of transfer reactions raises the question, if this is really caused by the

de-phasing of the associated scattering amplitudes or if those channels may be not affected by the barrier distribution of a reaction at all. For some systems it has been possible[16,17] to isolate the effects of particularly strong transfer channels on the barrier distribution and in principle there should be no difference in the way transfer channels couple to the relative motion of the binary system. Thus one may expect to see some experimental evidence for the barrier distribution in transfer excitation functions.

It is well known that excitation functions for transfer reactions have a bell-like shape which is roughly centered at the energy corresponding to the height of the potential barrier. Following the spirit of the previous sections one may therefore define the peaked function

$$G^{trans}(E, B_k) \equiv \frac{1}{g_0(B_k)} \frac{d\sigma^{trans}}{d\sigma^R}(E, B_k) \tag{3.21}$$

where $d\sigma^{trans}/d\sigma^R(E, B_k)$ is the excitation function of a transfer reaction for a potential barrier B_k and

$$g_0(B_k) \equiv \int_0^\infty \frac{d\sigma^{trans}}{d\sigma^R}(E, B_k)dE \tag{3.22}$$

is a normalization constant. If it is then assumed that there exists a distribution $D(E, B_k)$ of such potential barriers B_k and that for each barrier the transfer probability is proportional to the barrier weight W_k, the distribution

$$D^{trans}(E) \equiv \frac{1}{\hat{g}_0} \frac{d\sigma^{trans}}{d\sigma^R}(E) = \sum_{k=0}^{n} W_k G^{trans}(E, B_k) \tag{3.23}$$

with

$$\hat{g}_0 \equiv \int_0^\infty \frac{d\sigma^{trans}}{d\sigma^R}(E)dE \tag{3.24}$$

should be a representation of the barrier distribution.

These qualitative arguments have been tested for the systems ^{16}O + ^{144,154}Sm, ^{186}W using the measured excitation functions for scattered nuclei with $Z = 8, 7$ and 6 which are displayed in Figures 3.3 and 3.4 and tabulated in Tables A.3–A.7 in the Appendix. These excitation functions may be associated with certain transfer reactions which dominate the measured cross sections. The excitation function for scattered nuclei with $Z = 8$ consists, if the elastic events are subtracted, mainly

[16]C.R. Morton *et al.*, Phys. Rev. Lett. **72** (1994) 4074.

[17]A.M. Stefanini *et al.*, Phys. Rev. C **52** (1995) R1727.

of neutron transfer reactions. The excitation function for $Z = 7$ represents proton transfer reactions. Finally, the excitation function for $Z = 6$ comprises two proton and α-transfer reactions. These three excitation functions have been transformed according to Equation 3.23 to yield the distributions $D^{trans}(E)$. The normalization constant $\hat{g}_0$ has been chosen, so that the integral of $D^{trans}(E)$ is unity. The distributions $D^{trans}(E)$ are displayed in Figure 3.11 where they are compared with the barrier distribution representations $D^{fus}(E)$ from fusion.

Despite the gross approximations and the large width of the bell-like function $G^{trans}(E, B_k)$, it is found that in particular at the lower energies the shapes of the four independent representations of the barrier distribution are correlated. This may be interpreted as experimental evidence that the barrier distribution affects the transfer channels. It should be noted that the transfer excitation functions are manipulated differently to yield the barrier distribution representation $D^{qel}(E)$ than to give $D^{trans}(E)$. This is a consequence of the different approximations involved in the derivations of these two representations.

3.3 Preliminary Summary

The results of the experimental test of the suggested technique to extract the barrier distribution from quasi-elastic scattering excitation functions may be summarized as follows. In order to avoid distortions due to Fresnel diffraction backward angle measurements are best suited for this technique. Nevertheless for the reactions ^{16}O + ^{154}Sm and ^{16}O + ^{186}W oscillations reminiscent of Fresnel diffraction have been observed even at $\theta_{lab} = 170°$. Such oscillations may be avoided for heavier system with larger Sommerfeld parameters.

The measured quasi-elastic excitation functions decrease smoothly with energy. The rate of decrease is different for each reaction, reflecting the structure of the reactants. This enables the extraction of the barrier distribution representations $D^{qel}(E)$ which are qualitatively similar to the representation $D^{fus}(E)$ obtained from fusion excitation functions. However, it is found that the width of an individual peak in the distribution $D^{qel}(E)$ is larger than in $D^{fus}(E)$, making the new representation less sensitive to the barrier structure.

At energies below the average fusion barrier the barrier distribution representation $D^{qel}(E)$ agrees with $D^{fus}(E)$ in the prediction of the barrier structure. However, at the higher energies the new representation appears to be distorted. This

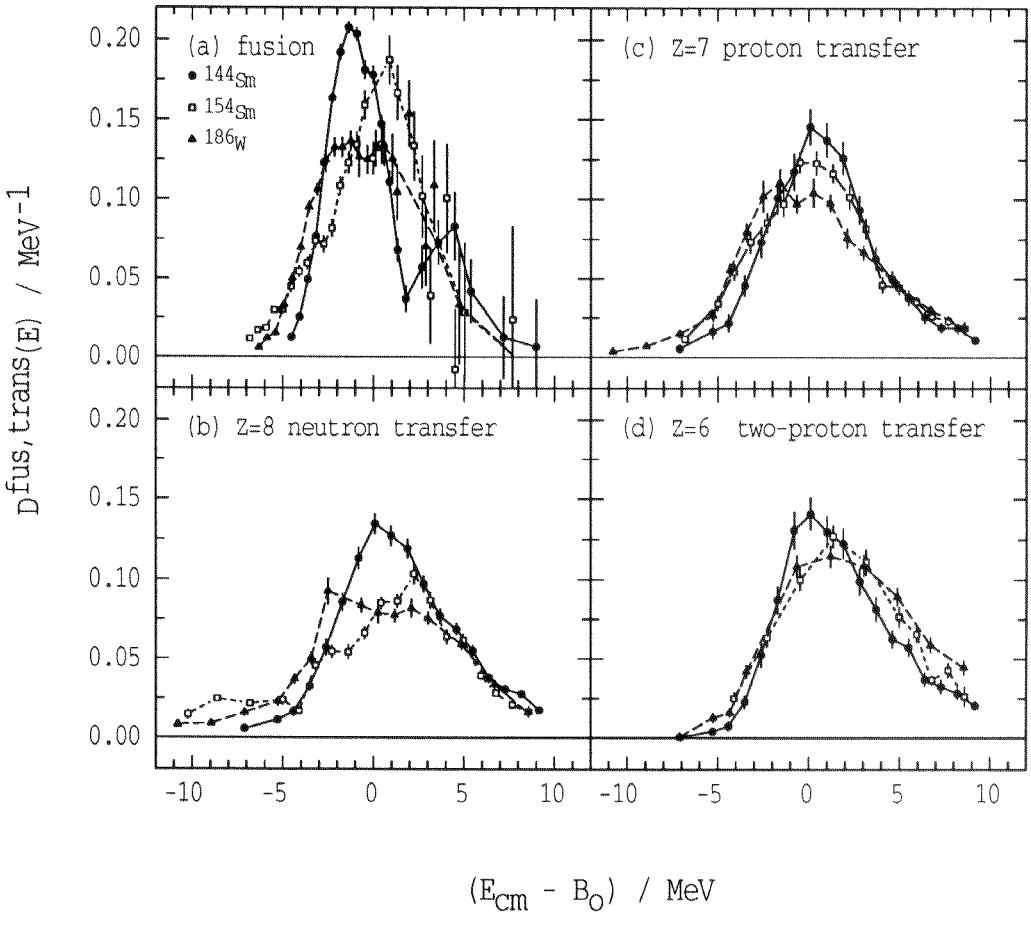

Figure 3.11: *Barrier distribution representations $D^{fus}(E)$ and $D^{trans}(E)$ for the systems ^{16}O + ^{144}Sm, ^{154}Sm and ^{186}W from fusion and transfer excitation functions. The distributions $D^{trans}(E)$ have been extracted from the excitation functions for (b) scattered nuclei with $Z = 8$ which is dominantly neutron transfer, for (c) scattered nuclei with $Z = 7$ which is largely proton transfer and for (d) scattered nuclei with $Z = 6$ which is α- and two-proton-transfer. B_0 is the appropriate average potential barrier. Data points for the same system have been connected to facilitate the comparison.*

seems to be caused by the many residual channels not included in the coupling matrix. The residual channels, which are dominantly transfer reactions, dominate the quasi-elastic scattering cross section at the higher energies. For transfer reactions the sudden and the iso-centrifugal approximations, which are both implicit in the derivation of $D^{qel}(E)$, are often not good. Large absolute Q-values and large changes in angular momentum during the interaction can, however, lead to considerable de-phasing of the corresponding scattering amplitudes. It is then likely that the information about the barrier structure is lost when these channels are combined as quasi-elastic cross section.

The distributions $D^{qel}(E)$ may be useful in the determination of the barrier distribution for systems which have pronounced barrier structure below the average barrier. A system where this might be expected is ^{40}Ca + ^{96}Zr which has several strong positive Q-value transfer channels. Such channels can lead to detailed barrier structure at low energies. Among other interesting questions this expectation motivated a follow-up experiment to measure the distributions $D^{qel}(E)$ and $D^{fus}(E)$ for the two reactions ^{40}Ca + ^{90,96}Zr. The quasi-elastic scattering results of this experiment are discussed in Section 3.5.

Two more experiments have been carried out utilizing the reactions of ^{16}O and ^{32}S with ^{208}Pb. Both reactions have larger products of charges Z_pZ_t than the oxygen reactions discussed in the previous sections. This leads to larger coupling matrix elements $M_{ji}(r)$ for collective excitations, as seen from Equation 1.53. Also, the Sommerfeld parameters for these reactions are larger. Consequently, as illustrated in Figure 1.15, diffraction effects should be reduced. Due to the larger matrix elements, potential barriers associated with collective excitations of the reactants should be further apart in barrier height than in the reactions investigated thus far. A larger separation of the barriers may enable them to be resolved in $D^{qel}(E)$ despite the large peak width and the distortions at higher energies due to transfer channels. The measurements of the distributions $D^{qel}(E)$ for these two systems are discussed in the following section.

3.4 The Systems ^{16}O, ^{32}S + ^{208}Pb

The quasi-elastic scattering excitation functions at $\theta_{lab} = 170°$ for the systems ^{16}O + ^{208}Pb and ^{32}S + ^{208}Pb were measured using ^{16}O and ^{32}S beams in the energy range $E_{lab} = 69 - 90$ MeV and $E_{lab} = 140 - 183$ MeV, respectively. The beams

were provided by the tandem accelerator of the Australian National University. The targets were 1 mm wide strips of lead, evaporated onto an aluminium backing. In the ^{16}O experiment the target thickness was 40 μg/cm^2, whereas in the ^{32}S experiment it was 100 μg/cm^2 The experimental set-up has been described in Section 2.4.

The experiments yielded excitation functions for quasi-elastic relative to Rutherford scattering. The quasi-elastic scattering cross sections comprise all elastic, inelastic and transfer events. The set-up allowed the atomic numbers of the scattered projectile-like nuclei to be identified. Thus in addition, excitation functions for scattered nuclei with the atomic numbers Z = 8, 7 and 6 for the ^{16}O reaction and with the atomic numbers Z = 16, 15 and 14 for the ^{32}S reaction were measured. In the energy spectra for the Z = 8 and Z = 16 events, the elastic scattering peaks could be isolated. This allowed the extraction of elastic scattering excitation functions. In the case of ^{32}S + ^{208}Pb the elastic peak was, however, contaminated by events associated with positive Q-value neutron transfer channels. The measured excitation functions are documented in the Appendix in Tables A.8 and A.12 and they are displayed in Figure 3.12. The figure shows that the relative contributions of the elastic and the combined inelastic and transfer cross sections to the quasi-elastic scattering cross section are different for the two systems. For the sulphur reaction the elastic scattering cross section falls off quickly with increasing energy, so that inelastic and transfer processes account for a much larger part of the quasi-elastic cross section, than in the oxygen reaction.

The quasi-elastic scattering excitation functions have been transformed into the barrier distribution representations $D^{qel}(E)$ using Equation 3.15. The distributions $D^{qel}(E)$ of the two systems resulting from energy steps ΔE_{lab} =2 MeV, 3 MeV and 4 MeV in Equation 3.15 are shown in Figure 3.13. For both systems the three distributions $D^{qel}(E)$ are consistent with each other. For ^{16}O + ^{208}Pb the distributions $D^{qel}(E)$ show a single peak with a tail on the high energy side. For ^{32}S + ^{208}Pb they are broader with two slight indications of structure at 140 MeV and 142 MeV.

The distributions $D^{qel}(E)$ obtained with ΔE_{lab} = 2 MeV are compared with the corresponding distributions $D^{fus}(E)$ from fusion data in Figure 3.14. The fusion data for the oxygen reaction have been taken from other work[18], whereas the data for the sulphur reaction have been measured in this work, see Chapter 6. The energies for $D^{qel}(E)$ have been reduced by the centrifugal energy as given

[18]C.R. Morton *et al.*, Phys. Rev. C **52** (1995) 243.

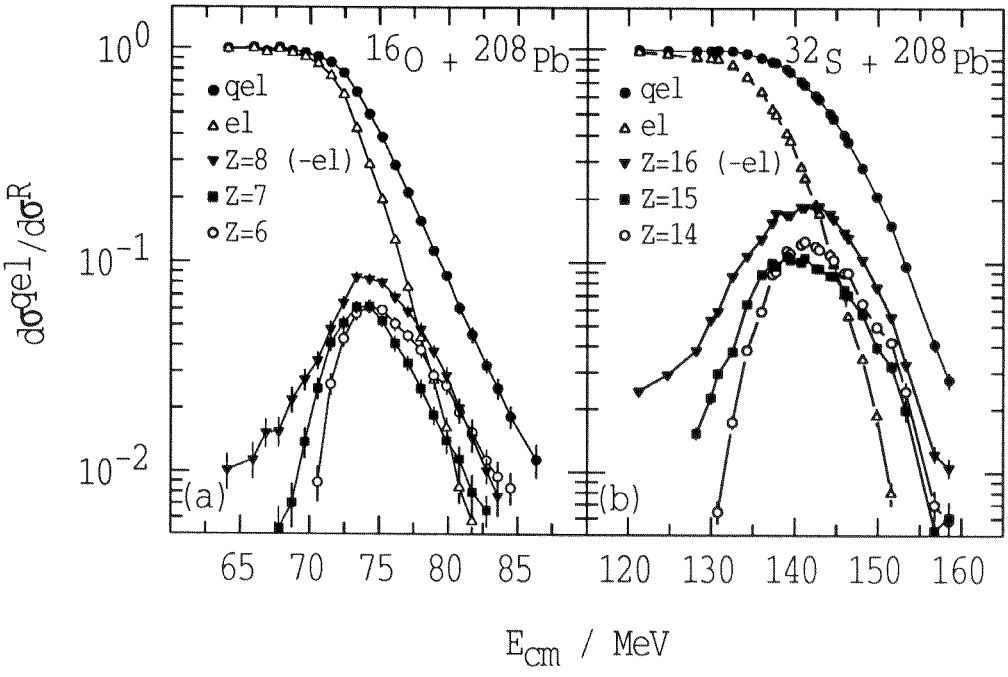

Figure 3.12: *The ratio of the measured differential quasi-elastic (qel), elastic (el) and transfer cross sections relative to Rutherford scattering for (a) ^{16}O + ^{208}Pb and (b) ^{32}S + ^{208}Pb at θ_{lab} = 170°. The quasi-elastic scattering events could be separated according to the atomic number Z of the scattered nuclei. The symbol (-el) indicates that the excitation function does not include the elastic scattering.*

by Equation 3.16. The distributions $D^{fus}(E)$ have been divided by the classical fusion cross section πR_0^2, which has been determined from the first differential of $E\sigma^{fus}$ with respect to energy. For the sulphur system the fusion data have been supplemented at high energies with data points obtained using ΔE_{lab} = 4 MeV in the point-difference formula. For both systems the distributions $D^{qel}(E)$ and $D^{fus}(E)$ are qualitatively similar. As before the representations $D^{qel}(E)$ fall off smoothly at the higher energies.

Of particular interest is the system ^{32}S + ^{208}Pb for which $D^{fus}(E)$ shows pronounced structure. There is a slight, but unambiguous indication of the barrier structure at the lower energies also in $D^{qel}(E)$. At the higher energies $D^{fus}(E)$ is not well defined, however, it shows a peak at $E_{cm}/B_0 \simeq 1.05$ with a width which would be consistent with that expected for a barrier. As the high energy peak in the barrier distribution of ^{16}O + ^{144}Sm, this structure is not resolved in $D^{qel}(E)$.

It may be summarized that the study of the reactions ^{16}O, ^{32}S + ^{208}Pb confirms

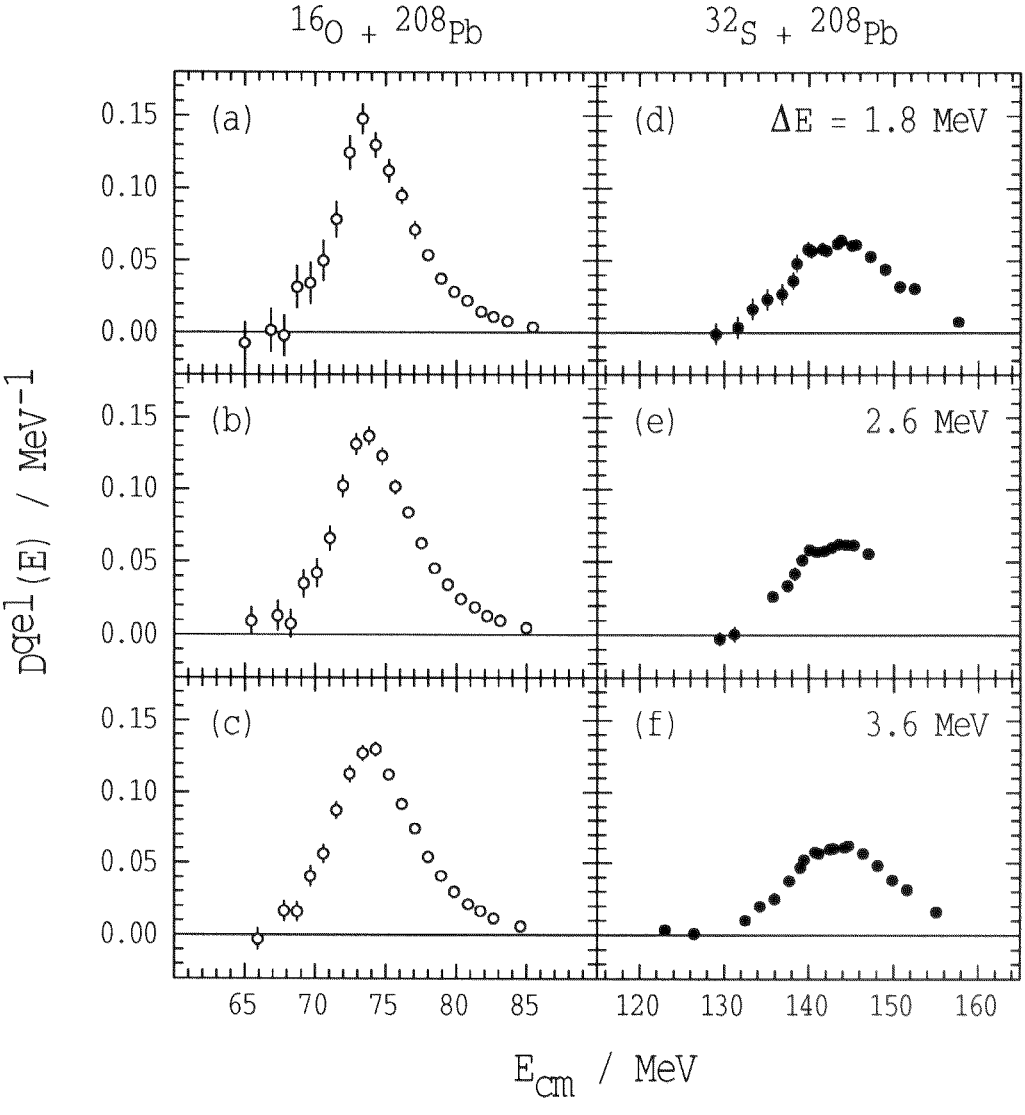

Figure 3.13: *Representations $D^{qel}(E)$ of the barrier distributions for $^{16}O + ^{208}Pb$ (a–c) and $^{32}S + ^{208}Pb$ (d–f). A typical value for the energy step ΔE_{cm} as used in the point-difference formula is given in the figure for adjacent panels. In panel (e) there is no data at the higher energies, because the cross sections have only been measured in steps of $\Delta E_{lab} = 2$ MeV.*

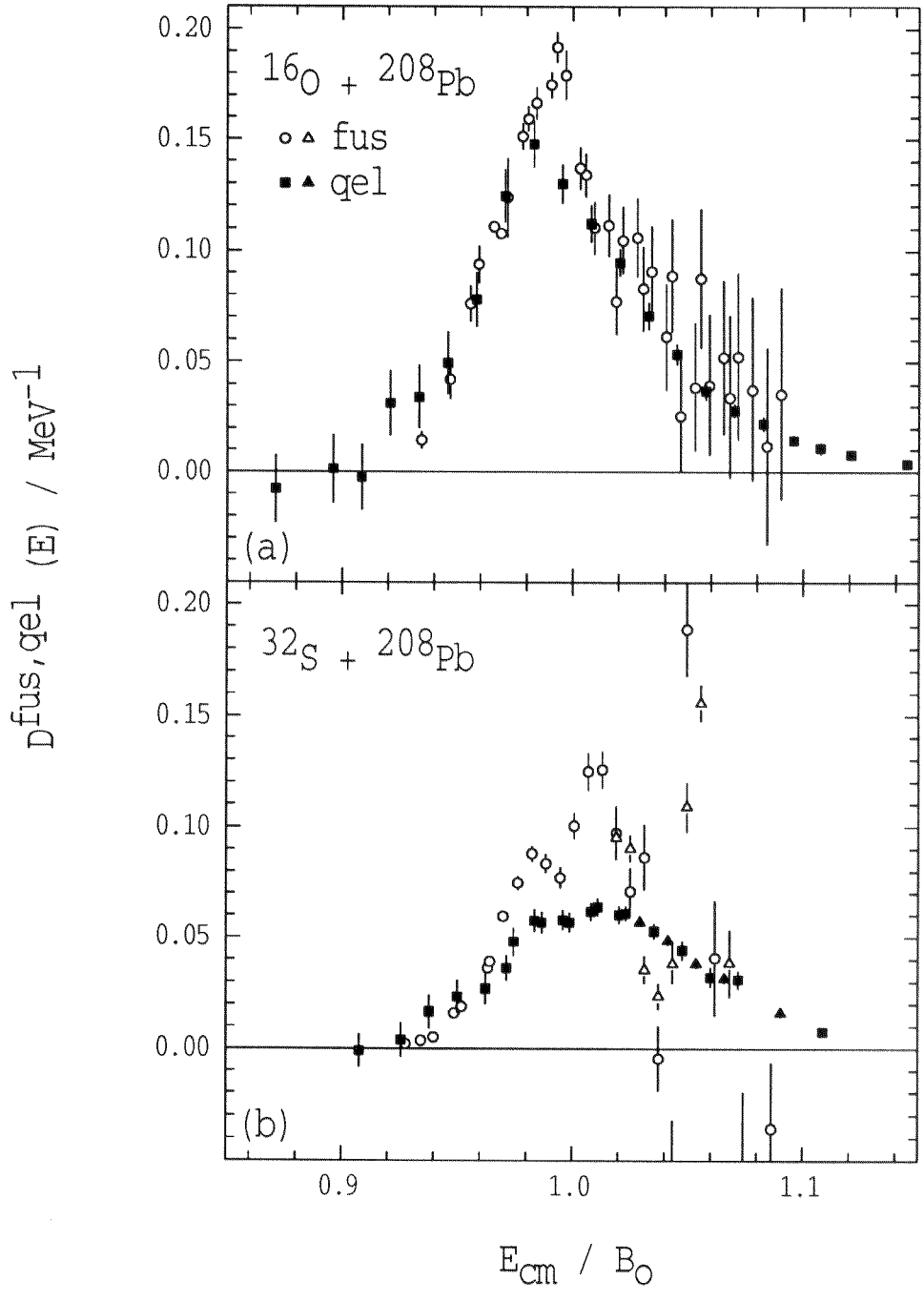

Figure 3.14: *The distributions $D^{fus}(E)$ and $D^{qel}(E)$ as extracted from experimental data for (a) $^{16}O + ^{208}Pb$ and (b) $^{32}S + ^{208}Pb$. The energy scale is given in units of the one-dimensional barrier B_0, with $B_0 = 74.5$ MeV for the lighter and $B_0 = 142.0$ MeV for the heavier system, respectively.*

the earlier results. For both systems the distributions $D^{qel}(E)$ and $D^{fus}(E)$ are qualitatively similar. The featureless, smooth tail of $D^{qel}(E)$ at the higher energies persists even in these heavier systems, which should be less affected by diffraction effects. This supports the view that the smooth tail, as suggested above, is due to the de-phasing of the scattering amplitudes and not caused by diffraction, as could have been argued. As for the other systems, barrier structure present at energies below the average barrier B_0 is reflected in $D^{qel}(E)$, although the resolution is not as good as in $D^{fus}(E)$.

3.5 The Systems ^{40}Ca + ^{90,96}Zr

Since the experimental distributions $D^{qel}(E)$ are sensitive to the barrier distribution of a reaction at energies below the average potential barrier, they should be particularly useful for systems which show complicated barrier structures at such energies. This can be the case for systems with rotational nuclei, as the comparison of the reactions ^{16}O + ^{154}Sm and ^{16}O + ^{186}W shows[19]. For systems with vibrational nuclei, however, detailed barrier structure occurs typically at the higher energies. The system ^{16}O + ^{144}Sm is a textbook example of this situation. In contrast, coupling to positive Q-value channels, such as nucleon transfer reactions, can result in interesting barrier structure at the lower energies. This is shown in Figure 1.12 for a single positive Q-value channel. Systems which are dominated by positive Q-value transfer channels may therefore be studied satisfactorily by extracting the barrier distribution from its representation $D^{qel}(E)$.

A reaction which has several strong positive Q-value transfer channels is the system ^{40}Ca + ^{96}Zr. This is shown in Table 3.2, where the Q-values of these channels are compared with the equivalent ones for the reaction ^{40}Ca + ^{90}Zr. Whilst the two zirconium target nuclei are very similar in their nuclear structure properties, as illustrated in Figure 1.3, their neutron transfer Q-values differ distinctively when they are combined with ^{40}Ca. In the heavier system up to 8 neutrons can be transferred from ^{96}Zr to ^{40}Ca with positive Q-values. In contrast, the Q-values for the corresponding channels in the lighter system are all negative. Thus, these two reactions appear to be ideally suited for a study based on the barrier distribution representation $D^{qel}(E)$.

However, in order to obtain a complete picture, both fusion and quasi-elastic

[19]J.R. Leigh *et al.*, Phys. Rev. C 47 (1993) R437.

Q-values for simultaneous transfer / MeV		
^{40}Ca + xn	^{90}Zr − xn	^{96}Zr − xn
1n	−3.611	+0.509
2n	−1.445	+5.525
3n	−5.861	+5.239
4n	−4.170	+9.637
5n	−9.658	+8.417
6n	−9.038	+11.617
7n	−14.928	+6.919
8n	−15.225	+7.549

Table 3.2: *The Q-values for pick-up of x neutrons by the ^{40}Ca projectile from the target nuclei ^{90}Zr and ^{96}Zr. The values are for simultaneous transfer between the ground states.*

scattering have been measured for these systems. The fusion measurements, the extracted distributions $D^{fus}(E)$ and their interpretation are discussed in Chapter 5. This section describes the extraction of the distributions $D^{qel}(E)$ from the quasi-elastic scattering data. The distributions $D^{qel}(E)$ are compared with the results for $D^{fus}(E)$. Using both representations the strongest potential barriers are then determined empirically within the eigen-channel model.

3.5.1 Experimental Data

The quasi-elastic scattering excitation functions $d\sigma^{qel}/d\sigma^{R}(E)$ for the systems ^{40}Ca + ^{90,96}Zr have been measured at a centre-of-mass angle $\theta_{cm} = 136°$ in parallel with the fusion excitation functions, as described in Section 2.4. The experimental data are tabulated in the Appendix in Table A.10 and they are shown in Figure 3.15. In order to remove differences due to the different sizes of the target nuclei, the excitation function for ^{40}Ca + ^{96}Zr in Figure 3.15 has been normalized to the one for ^{40}Ca + ^{90}Zr by multiplying the energies with the ratio of the average barriers B_0 of the two systems, which is 1.013. The values for B_0 have been extracted from the fusion excitation functions. This manipulation of the data for ^{40}Ca + ^{96}Zr is maintained throughout Section 3.5.

The two quasi-elastic scattering excitation functions in Figure 3.15 have been differentiated with respect to energy using the point-difference formula given in

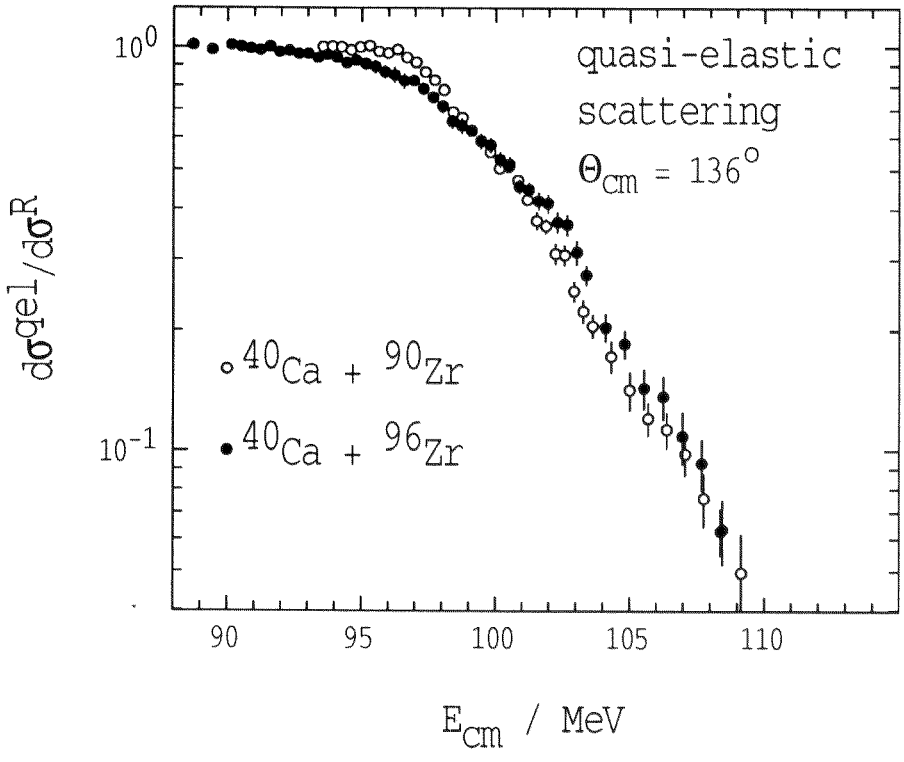

Figure 3.15: *The excitation functions for quasi-elastic scattering at θ_{cm} = 136° relative to Rutherford scattering. The excitation function for $^{40}Ca + ^{96}Zr$ has been normalized to the one for $^{40}Ca + ^{90}Zr$ as described in the text. Only statistical uncertainties are given.*

Equation 3.15. The barrier distribution representations $D^{qel}(E)$ for the two systems for energy step lengths of ΔE_{cm} = 1.75 MeV, 2.1 MeV and 2.8 MeV in the point-difference formula are shown in Figure 3.16. To facilitate a comparison with $D^{fus}(E)$, the energy scales have been reduced by the centrifugal energy E_{cent} as given by Equation 3.16.

For each system the experimental distributions $D^{qel}(E)$ for different ΔE_{cm} are consistent with each other and show the following features. In the case of ^{40}Ca + ^{90}Zr two peaks are present at $E_{cm} \simeq$ 95 MeV and 98 MeV. A third peak may be at $E_{cm} \simeq$ 103.5 MeV. The distribution for ^{40}Ca + ^{96}Zr is broader and flatter than the one for ^{40}Ca + ^{90}Zr. For both systems $D^{qel}(E)$ shows at the higher energies a smooth tail indicating the reduction in sensitivity discussed in Section 3.2.3.

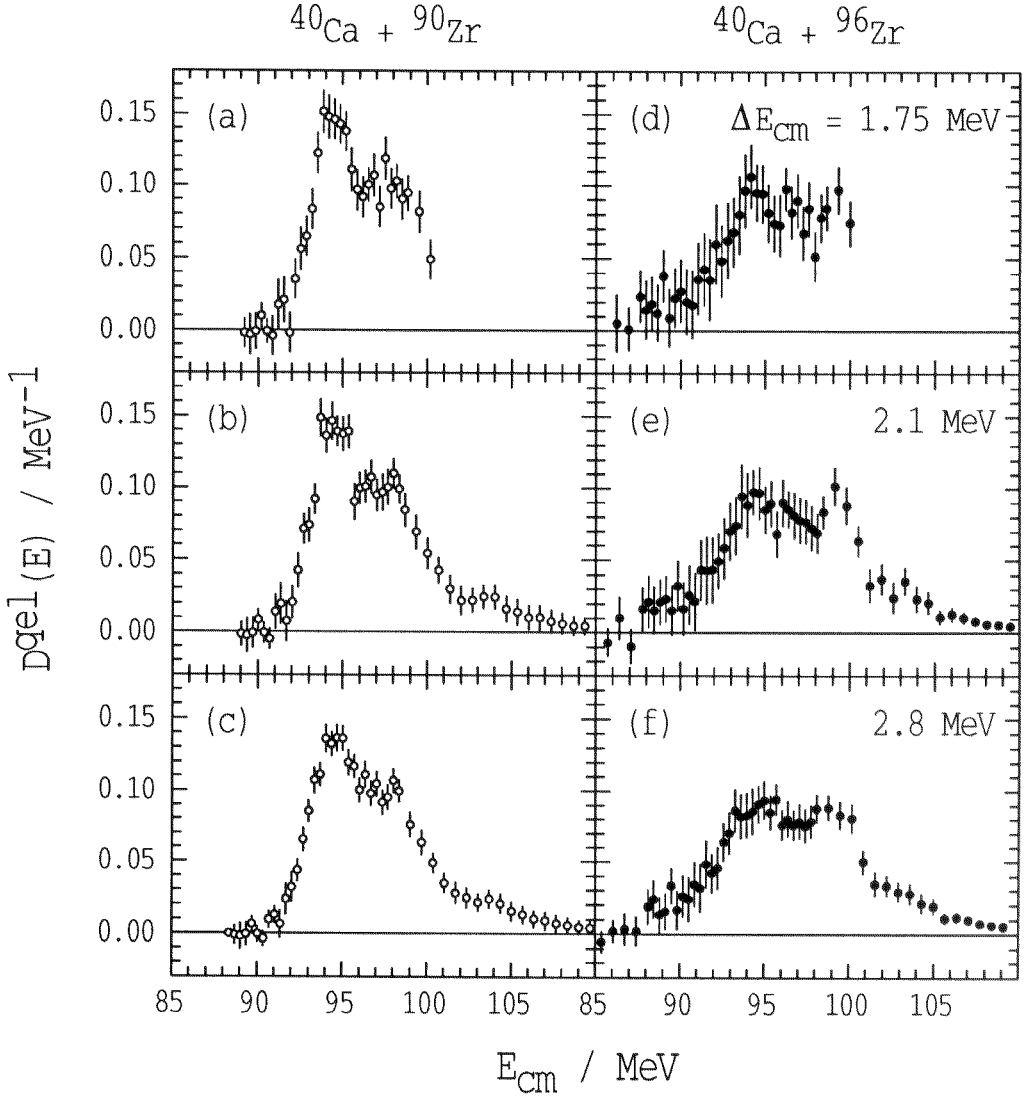

Figure 3.16: *Representations $D^{qel}(E)$ of the barrier distributions for $^{40}Ca + ^{90}Zr$ (a–c) and $^{40}Ca + ^{96}Zr$ (d–f). The energy steps ΔE_{cm} used in the point-difference differentiation are given in the figure for adjacent panels. The data in panels (a) and (d) are limited to the lower energies where the excitation functions have been measured in energy steps of 0.5 MeV in the laboratory system, whilst at the higher energies the energy step was 1 MeV.*

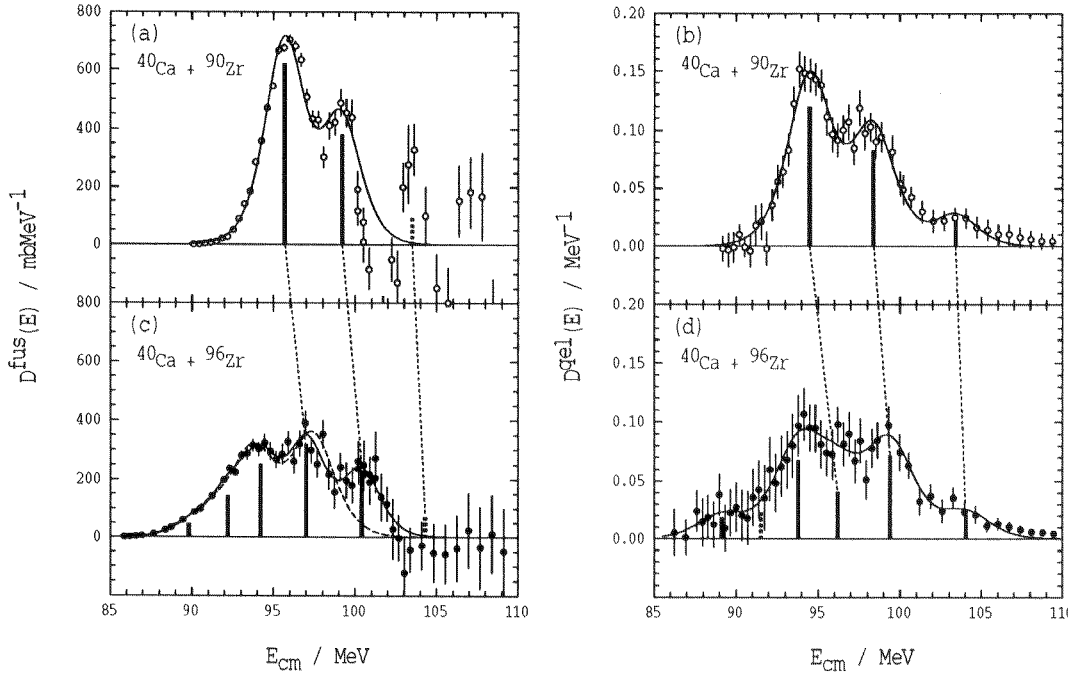

Figure 3.17: *Empirical analysis of the experimental barrier distribution representations $D^{fus,qel}(E)$ within the eigen-channel model. The best fits to the data are shown as solid curves. The long-dashed curve in panel (c) is a three barrier fit. The extracted fusion barriers are indicated as solid bars. Dashed bars are tentative. The dashed lines illustrate that the heavier system features at least three additional barriers at the lower energies.*

3.5.2 Empirical Interpretation

The experimental results have been analysed empirically within the eigen-channel model as described in Section 3.2.3. In order to achieve a good compromise between sensitivity and accuracy, the analysis focused on the experimental barrier distribution representations $D^{qel}(E)$ which result from using an energy step $\Delta E_{cm} = 1.75$ MeV in the point-difference formula given in Equation 3.15. These representations have been supplemented above $E > 100$ MeV with data points from the distributions with $\Delta E_{cm} = 2.1$ MeV. The distributions $D^{qel}(E)$ are compared in Figure 3.17 with the corresponding distributions $D^{fus}(E)$ from fusion, see Chapter 5. The potentials which are used there to reproduce the high energy fusion data for the two systems suggest a barrier curvature $\hbar\omega_0 \simeq 3.4$ MeV, so that the width of a single peak in $D^{fus,qel}(E)$ is of the order $0.56\ \hbar\omega_0 \simeq 1.9$ MeV. With $\Delta E_{cm} = 1.75$ MeV in the point-difference formula the width ΔB of a single peak

	^{40}Ca + ^{90}Zr				^{40}Ca + ^{96}Zr			
	fusion		quasi-elastic		fusion		quasi-elastic	
k	B_k	W_k	B_k	W_k	B_k	W_k	B_k	W_k
0	–	–	–	–	89.8	0.05	89.1	0.08
1	–	–	–	–	92.2	0.15	(91.5)	(0.10)
2	–	–	–	–	94.2	0.25	93.8	0.31
3	95.7	0.62	94.5	0.53	97.0	0.32	96.2	0.19
4	99.2	0.38	98.4	0.36	100.4	0.23	99.4	0.33
5	(103.5)	(0.10)	103.4	0.11	(104.0)	(0.05)	104.0	0.10
ΔB	2.8		3.2		2.7		3.5	

Table 3.3: *The heights B_k and weights W_k of the potential barriers for ^{40}Ca + ^{90,96}Zr as extracted from fits to the experimental distributions $D^{fus,qel}(E)$. The quantity ΔB is the width of a single peak in $D^{fus,qel}(E)$. Brackets indicate tentative assignments. Energies are given in MeV. Uncertainties are not indicated for the sake of clarity.*

in the experimental distributions $D^{fus,qel}(E)$ may be estimated to be

$$\sqrt{(1.9 \text{ MeV})^2 + (1.75 \text{ MeV})^2} \simeq 2.6 \text{ MeV} \tag{3.25}$$

The distributions $D^{fus,qel}(E)$ have been fitted with Equation 3.18 for different n by varying the heights and weights of the barriers. The best fits are shown in Figure 3.17 and the extracted barriers are tabulated in Table 3.3. For the system ^{40}Ca + ^{90}Zr the distribution $D^{fus}(E)$ can be reproduced below $E_{cm} = 102$ MeV with the two barriers indicated in Figure 3.17(a) as solid bars and a barrier width $\Delta B \simeq 2.8$ MeV which is close to the expected value. Above $E_{cm} = 102$ MeV a sensible fit was impossible because of the large fluctuations. However, it seems reasonable to assume the presence of a third barrier with a height of 103.5 MeV and an approximate weight of 0.1. This three-barrier-structure is confirmed by the fit to $D^{qel}(E)$ for this system which is displayed in Figure 3.17(b). Similar to what has been found in Section 3.2.3, the width ΔB of a single peak in $D^{qel}(E)$ is larger than in $D^{fus}(E)$. The weights W_k of the three barriers extracted from the fit to $D^{qel}(E)$ are very similar to the results from fusion, whereas the heights B_k tend to be lower by approximately 1 MeV.

For the system ^{40}Ca + ^{96}Zr a three-barrier-fit of $D^{fus}(E)$ over-predicts ΔB and does not reproduce the data, as is shown in Figure 3.17(c) by the long-dashed

curve. It was found that five barriers are necessary to achieve agreement resulting in $\Delta B \simeq 2.7$ MeV. The extracted barrier structure is indicated in the figure and given in Table 3.3. The five-barrier-fit of $D^{qel}(E)$ for this system, which is shown in Figure 3.17(d), extracts a similar barrier structure with $\Delta B \simeq 3.5$ MeV. There are, however, two differences. Firstly, the second lowest barrier ($k = 1$) is not confirmed, instead the fit predicts a 104 MeV barrier ($k = 5$). Secondly, the barrier with a height of ~ 97 MeV ($k = 3$) is not weighted as much as expected from the fusion fit. Considering the experimental uncertainties the slightly different results for $D^{fus}(E)$ and $D^{qel}(E)$ can best be reconciled by assuming six barriers to be present. These include the five as extracted by the fit of $D^{fus}(E)$ and a sixth barrier at 104 MeV with an approximate weight of 0.1, as seen in $D^{qel}(E)$. As previously, the peak width ΔB is larger for the fits to the experimental distributions $D^{qel}(E)$ than for the fits to $D^{fus}(E)$.

For both systems a close inspection of $D^{fus}(E)$ and $D^{qel}(E)$ reveals a systematic mismatch in energy of about 800 keV. The reason for this is not clear. Since the energies of the quasi-elastic data have been reduced by the centrifugal energy which is of the order of 4 MeV, an overestimation of this energy shift could be a possible cause for the mismatch. Correcting for the mismatch further improves the good agreement between the barrier structures extracted from $D^{fus}(E)$ and $D^{qel}(E)$.

A comparison of the barrier structures for the two systems as extracted from the fits and tabulated in Table 3.3 shows that above $E_{cm} \simeq 95$ MeV the structures are similar, consisting of three barriers. This is indicated in Figure 3.17 by the dashed lines. Below $E_{cm} \simeq 95$ MeV no other barriers are present in the reaction ^{40}Ca + ^{90}Zr, whereas for ^{40}Ca + ^{96}Zr three additional barriers exist. This marks an important difference between the two systems. The two barrier distributions are discussed further and interpreted with the help of coupled-channels calculations in Chapter 5.

3.6 Concluding Remarks

The technique presented in this chapter enables the extraction of of a representation of the barrier distribution from backward angle quasi-elastic scattering excitation functions. For all systems investigated these barrier distribution representations are consistent with the representations from fusion, if diffraction effects and distortions due to the de-phasing of the various scattering amplitudes at energies above the

average barrier are taken into account. This confirms the view that fusion and quasi-elastic scattering are two complementary channels of the same physical problem and should thus be treated within a common model. The representations $D^{qel}(E)$ can be successfully applied in studies of barrier distributions in which the important barrier structures are at energies below the average potential barrier. This has been demonstrated for the systems ^{40}Ca + ^{90,96}Zr for which the distribution $D^{qel}(E)$ contains essentially the same information as $D^{fus}(E)$. In general, the information contained by $D^{qel}(E)$, particularly at the lower energies, is an independent check of the barrier structure revealed by the distribution $D^{fus}(E)$.